ARTICLES
https://doi.org/10.1038/s41556-019-0358-6
nature cell biology

Migrasomes provide regional cues for organ morphogenesis during zebrafish gastrulation

Dong Jiang[1,2,5], Zheng Jiang[1,5], Di Lu[1,2], Xuan Wang[1,2], Haisha Liang[1,2], Junfeng Zhang[1], Yaping Meng[1], Ying Li[1,2], Danni Wu[1,2], Yuwei Huang[1,2], Yuling Chen[3], Haiteng Deng[3], Qing Wu[4], Jingwei Xiong[4], Anming Meng[1*] and Li Yu[1,2*]

Migrasomes are recently identified vesicular organelles that form on retraction fibres behind migrating cells. Whether migrasomes are present in vivo and, if so, the function of migrasomes in living organisms is unknown. Here, we show that migrasomes are formed during zebrafish gastrulation and signalling molecules, such as chemokines, are enriched in migrasomes. We further demonstrate that Tspan4 and Tspan7 are required for migrasome formation. Organ morphogenesis is impaired in zebrafish MZ*tspan4a* and MZ*tspan7* mutants. Mechanistically, migrasomes are enriched on a cavity underneath the embryonic shield where they serve as chemoattractants to ensure the correct positioning of dorsal forerunner cells vegetally next to the embryonic shield, thereby affecting organ morphogenesis. Our study shows that migrasomes are signalling organelles that provide specific biochemical information to coordinate organ morphogenesis.

The exquisite morphogenesis of metazoan embryos requires mechanisms to integrate and relay spatio–temporal and specific chemical information among communities of moving cells. The combinatorial regulation of morphogenetic gradients is a well-established principle for pattern formation during embryogenesis[1] but additional mechanisms may still be undiscovered.

The migrasome is a newly discovered organelle in migrating cells[2]. During cell migration, projections named retraction fibres are pulled from the tails of cells. Migrasomes with a diameter of up to several micrometres grow on the retraction fibres. When a cell migrates away, the retraction fibres break down to leave the migrasomes behind. The migrasomes then rupture and release their contents into the environment in a process named migracytosis[2]. The physiological function of migrasomes in living animals is unknown at present.

Studying the physiological function of migrasomes is challenging because there are no in vivo models. We do not know where, when and in which kind of organism migrasomes may exist. As the only way to visualize migrasomes is through microscopic observation, we need a model system in which high-quality live imaging is possible. Another consideration is that migrasome formation is dependent on cell migration; thus, we need a model system with prominent cell migration. Based on these criteria, we chose the zebrafish embryo as a model system, as its optical clarity and out-of-mother development facilitate high-quality imaging[3,4] and the robust movement of cells during gastrulation makes it an ideal candidate for the investigation of migrasomes[5].

Results

Formation of migrasomes during gastrulation. To examine whether migrasomes exist in vivo, we observed shield-stage zebrafish embryos by differential interference contrast microscopy. We found numerous cellular projections in the extracellular spaces, with many vesicles attached to the projections (Fig. 1a). We previously identified Tspan4 as a migrasome marker[2]. To investigate the nature of the vesicles and processes, we injected *tspan4a–green fluorescent protein* (*GFP*) messenger RNA into one blastomere of individual embryos at the eight-cell stage to allow clonal labelling. At the shield stage, we observed numerous vesicles positive for Tspan4a–GFP that were connected to projections (Fig. 1b and Supplementary Video 1), similar to retraction fibres and migrasomes in mammalian cells cultured in vitro (Fig. 1c). To further characterize these vesicles and long projections, we carried out time-lapse imaging analysis of gastrulas expressing Tspan4a–GFP. The results revealed that these structures almost invariably appear on the side of the cell body opposite to the direction of migration (Fig. 1d), indicating that they are left by the migrating cells. More detailed time-lapse imaging analysis showed that, when cells are migrating away, the vesicles become detached from the projections and are left behind (Fig. 1e and Supplementary Video 2), which is a characteristic feature of migrasome biogenesis. In addition, we found abundant unattached extracellular Tspan4–GFP-positive vesicles (Fig. 1f). The GFP intensity and diameter in a single optical section of these vesicles are comparable to those in the connected vesicles (Fig. 1g). This observation suggests that these unattached vesicles are probably migrasomes that have disconnected from retraction fibres. In addition to Tspan4, integrin proteins have been shown to be enriched in migrasomes[6]. We observed the enrichment of Integrin β1 on these vesicles (Supplementary Fig. 1a,b), further supporting the idea that they are most probably migrasomes.

To avoid potential artefacts caused by the overexpression of functional proteins, we screened non-functional protein domains, which have previously been used to label membrane compartments. We identified the pleckstrin homology (PH) domain fused to mCherry

[1]State Key Laboratory of Biomembrane and Membrane Biotechnology, Tsinghua University–Peking University Joint Center for Life Sciences, School of Life Sciences, Tsinghua University, Beijing, China. [2]Beijing Frontier Research Center for Biological Structure, Beijing, China. [3]MOE Key Laboratory of Bioinformatics, School of Life Sciences, Tsinghua University, Beijing, China. [4]Beijing Key Laboratory of Cardiometabolic Molecular Medicine, Institute of Molecular Medicine, State Key Laboratory of Natural and Biomimetic Drugs, School of Pharmaceutical Sciences, Peking University, Beijing, China. [5]These authors contributed equally: Dong Jiang, Zheng Jiang. *e-mail: mengam@mail.tsinghua.edu.cn; liyulab@mail.tsinghua.edu.cn

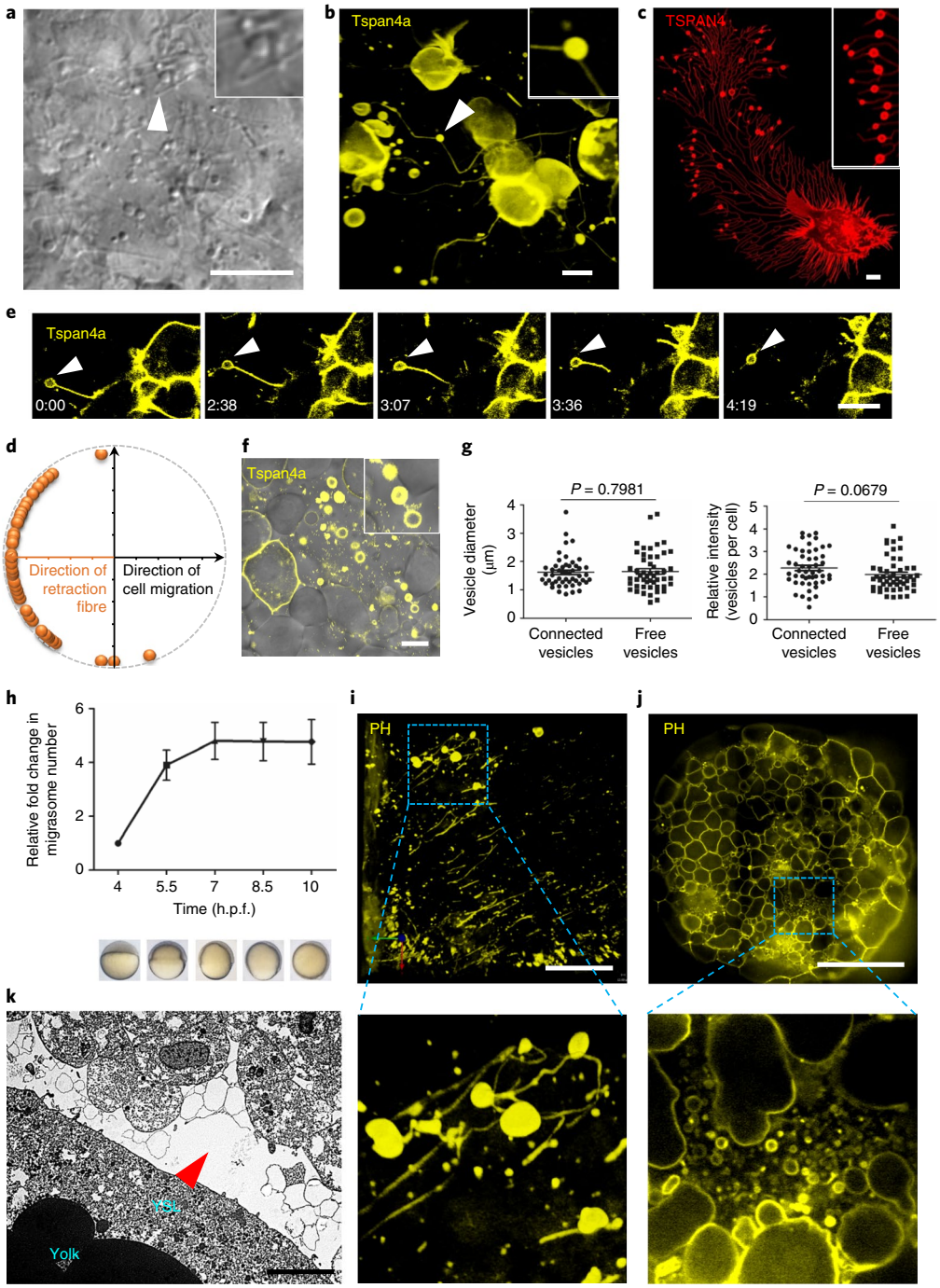

Fig. 1 | Formation of migrasomes during gastrulation. a, Differential interference contrast image of the vesicles and cellular processes in the extracellular spaces of a zebrafish embryo. The arrow indicates process-connected vesicles, magnified in the inset. **b**, Confocal image of migrasomes. A single blastomere of an embryo at the eight-cell stage was injected with *tspan4a–GFP* mRNA. Spinning disk microscopy was used to acquire 3D images of gastrula cells (6 h.p.f.). The arrow indicates an enlarged, process-connected vesicle. **c**, Migrasomes in cultured mammalian cells. L929 cells were transfected with *Tspan4–GFP* and observed by confocal microscopy. **d**, Zebrafish gastrulas were injected with *tspan4a–GFP* mRNA and subjected to time-lapse imaging. The position of the Tspan4a-positive cellular processes and vesicles relative to the direction of migration was analysed using Imaris software. $n = 50$ cells pooled from three independent experiments. **e**, Release of a Tspan4a-positive vesicle (indicated by the arrows) from a cell monitored by time-lapse microscopy. Time is in minutes and seconds. **f**, Differential interference contrast image of free migrasomes in a zebrafish gastrula. **g**, Diameter of free Tspan4a-positive vesicles (free vesicles) or process-connected Tspan4a-positive vesicles (connected vesicles). Data represent the mean ± s.e.m.; $n = 50$ vesicles per group pooled from two independent experiments. *P* values were calculated using a two-tailed, unpaired *t*-test. **h**, Migrasome formation along with development. A single blastomere of an embryo at the eight-cell stage was injected with *tspan4a–GFP* mRNA and 4D images (bottom) were later acquired by light-sheet microscopy. Data represent the mean ± s.e.m. (top); $n = 16$ embryos pooled from three independent experiments. **i**, Three-dimensional image of a network of projections and migrasomes inside a zebrafish gastrula. **j**, Migrasomes are enriched in pockets of extracellular space in gastrulas. The boxed areas in **i**,**j** are enlarged in the lower panels. **k**, TEM image of a vesicle-enriched pocket between the yolk syncytial layer (YSL) and mesendodermal cells. The arrow indicates a migrasome-enriched pocket. The experiments in **i**,**k** were performed twice. The experiments in **a**–**c**,**e**,**f**,**j** were repeated three independent times with similar results. The numerical source data for **g**,**h** are shown in Supplementary Table 3. Scale bars, 10 μm (**a**–**c**,**e**,**f**,**k**), 50 μm (**i**) and 100 μm (**j**).

as a marker for migrasomes in mammalian cells (Supplementary Fig. 1c). The PH–mCherry fusion protein was similarly enriched in Tspan4a-positive vesicles in zebrafish gastrulas (Supplementary Fig. 1d); moreover, the vesicles positive for PH–GFP were also positive for Integrin β1b (Supplementary Fig. 1e). Thus, PH–GFP can be used as a marker for further study. Next, we isolated embryonic cells from gastrulas and cultured them in a fibronectin-coated chamber. We found that the gastrula cells cultured in vitro are capable of generating migrasomes (Supplementary Fig. 1f).

Finally, we carried out transmission electron microscopy (TEM) analysis of zebrafish gastrulas and observed numerous membrane-bound vesicles with diameters ranging from 0.8 to 4 μm in the extracellular space (Supplementary Fig. 1g). To rule out the possibility that these vesicles are apoptotic bodies, we tested whether or not overexpression of Tspan4a and PH can induce apoptosis. We found that overexpression of GFP-tagged Tspan4a and PH does not enhance apoptosis (Supplementary Fig. 1h,i).

In summary, during zebrafish gastrulation, embryonic cells generate long projections and vesicles with a size, morphology, topology, molecular composition and biogenesis process similar to migrasomes on retraction fibres in cultured mammalian cells. We therefore believe that the long projections in zebrafish gastrulas are retraction fibres and the vesicles are migrasomes.

Temporal and spatial distribution of migrasomes in zebrafish embryos. We next investigated the temporal and spatial distribution of migrasomes during the early stages of embryonic development. For this purpose, we labelled migrasomes in embryos by overexpressing PH–GFP. We injected *PH–GFP* mRNA into only one blastomere of individual embryos in the eight-cell stage. The injected embryos were observed using four-dimensional (4D) imaging (Supplementary Fig. 1j) to count the number of migrasomes at each time point. This approach will underestimate the number of migrasomes, as only those generated from descendants of the mRNA-injected cell can be visualized. Using this method, we quantified the number of migrasomes in 16 embryos. We found that the migrasome number dramatically increased at 5.5 h post fertilization (h.p.f.) and peaked at 7 h.p.f., with no significant changes thereafter (Fig. 1h).

We then investigated the spatial distribution of migrasomes. We found that many migrasomes are enriched in pockets of extracellular space between the cells (Fig. 1i,j and Supplementary Videos 3–5). These extracellular spaces can be labelled by injecting fluorescently labelled dextrans (Supplementary Fig. 1k,l). Some pockets contained a dense network of migrasomes attached to the retraction fibres (Fig. 1i), whereas many migrasomes were disconnected from the retraction fibres in other pockets (Fig. 1j). Using TEM, we observed large pockets of extracellular space (Fig. 1k) that contained many vesicles or clusters of vesicles between the marginal mesendodermal cells next to the yolk syncytial layer. Finally, we investigated which cell types can generate migrasomes during gastrulation. We found that both mesodermal and endodermal cells are capable of generating migrasomes (Supplementary Fig. 1m,n).

In summary, large quantities of migrasomes form during gastrulation, and migrasomes are present in the extracellular pockets of the space between mesendodermal cells and in the pockets between the blastodermal margin and the yolk syncytial layer.

Tetraspanin 4a and 7, and Integrin β1b regulate migrasome formation in zebrafish gastrulas. We developed genetic models in which migrasome formation is blocked to study the physiological roles of migrasomes in zebrafish embryonic development. Recently, we reported that Integrin β1 is required for migrasome formation in mammalian cells cultured in vitro[6]. First, we confirmed the expression of *itgb1b* in early zebrafish embryos (Supplementary Fig. 2a). Although *itgb1b*$^{-/-}$ mutants are embryonically lethal, they can survive throughout the gastrulation stages, thus allowing the investigation of migrasome formation in *itgb1b*-deficient embryos during gastrulation. To quantify migrasome formation in zebrafish embryos, we carried out *z*-stack imaging of zebrafish gastrulas (Fig. 2a). Embryos derived from *itgb1b*$^{+/-}$ crosses were first analysed for the number of migrasomes and then individually genotyped. Similar to mammalian cells cultured in vivo[6], *itgb1b*$^{-/-}$ embryos formed significantly fewer migrasomes at the gastrulation stages (Supplementary Fig. 2b,c).

Integrin regulates migrasome formation by enabling cell migration and providing adhesion for the generation of retraction fibres. In mammalian cells, knocking down Integrin β1 impairs both cell migration and adhesion[7]; thus, we were not able to dissect the relative contribution of these two mechanisms. In agreement with previous publications[8], the speed of cell migration is not impaired in *itgb1b*$^{-/-}$ embryos during gastrulation (Supplementary Fig. 2d). This observation implies that Integrin β1b most probably regulates migrasome formation by providing adhesion.

Tetraspanins are a large family of transmembrane proteins that contain four transmembrane domains[9]. Tetraspanin 4 is enriched on migrasomes and has been identified as a marker for migrasomes. We speculate that tetraspanins may regulate migrasome formation. More than 40 *tetraspanin* genes have been annotated in the zebrafish[10]. We first checked the expression level of individual tetraspanins in zebrafish embryos at the shield stage through RNA sequencing (Fig. 2b). We selected *tspan7*, which has the highest expression level in zebrafish gastrulas, and *tspan4a*, which is the marker for migrasomes and is also expressed in zebrafish gastrulas, for further study. The expression of *tspan4a* and *tspan7* in gastrulas was verified by in situ hybridization (ISH; Supplementary Fig. 2e,f). Next, we knocked down *tspan4a* and *tspan7* using antisense morpholino oligonucleotides and quantified the number of migrasomes in *tspan4a* and *tspan7* morphants. We found that knockdown of *tspan4a* and *tspan7* indeed significantly blocked migrasome formation (Supplementary Fig. 2g–i). This result prompted us to generate *tspan4a*- and *tspan7*-knockout fish using clustered regularly interspaced short palindromic repeats (CRISPR)–CRISPR associated protein 9 (Cas9). Embryos homozygous for *tspan4a* and *tspan7* that had been derived from heterozygous crosses developed normally, probably due to the presence of their maternal products, and grew to adulthood. To completely eliminate any possible maternal effect, we performed self-crossing using *tspan4a*$^{-/-}$ or *tspan7*$^{-/-}$ adults to generate maternal-zygotic (MZ) mutants (Supplementary Fig. 2j). We found that the number of migrasomes was significantly decreased in MZ*tspan4a*- and MZ*tspan7*-mutant embryos at the shield stage (Fig. 2c–f), whereas the migration speed of cells in these mutants was not reduced (Fig. 2g).

Zebrafish organ morphogenesis is regulated by *tspan4a* and *tspan7*. We then analysed the phenotype of MZ*tspan4a*- and MZ*tspan7*-mutant embryos. First, we investigated whether gastrulation is affected in MZ*tspan4a*- and MZ*tspan7*-mutant embryos. We found that the overall gastrulation cell movements were not markedly altered in either mutant (Supplementary Fig. 3a–c). Moreover, we did not observe any obvious defects in the dorsal–ventral axis formation or convergence and extension (Supplementary Fig. 3d,e). These results indicate that gastrulation is largely normal in MZ*tspan4a*- and MZ*tspan7*-mutant embryos.

We next examined organ morphogenesis at 48 h.p.f. with ISH using markers for liver primodium (*cp*), pancreatic bud (*pdx1*), intestinal bulb and other endodermal derivatives (*foxa3*), heart tubes (*myl7*) and pronephric tubule (*slc20a1a*). We found that organ morphogenesis was impaired in the MZ*tspan4a* or MZ*tspan7* mutants. Many organs showed morphological deformation or were reduced in size (Fig. 3a); in addition, we noticed laterality defects

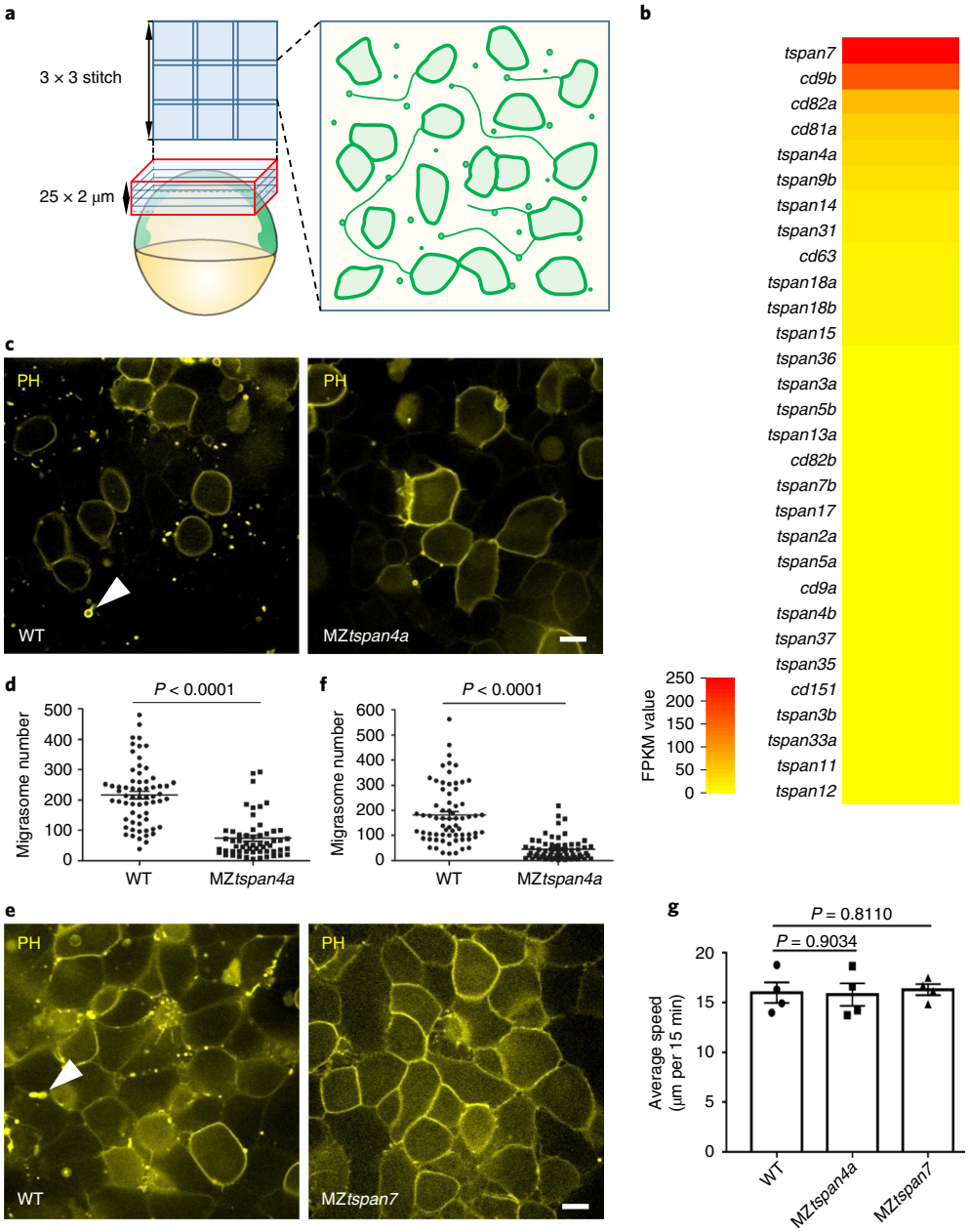

Fig. 2 | Tetraspanin 4a and 7 regulate migrasome formation in zebrafish gastrulas. a, Diagram showing how *z*-stack images were collected from zebrafish gastrulas for the quantification of migrasome number. Migrasomes labelled with PH–GFP were visualized in WT and *itgb1b* mutant gastrulas. The *z*-stack images of the gastrulas were acquired by spinning disk microscopy. Twenty-five slices were acquired at 2-μm intervals from the animal pole. Nine images were combined for each slice. **b**, Heat map of the expression levels of different *tspan* genes in zebrafish gastrulas measured through RNA sequencing. The experiment was done once. FPKM, fragments per kilobase million. **c**,**e**, Representative images of migrasomes in WT and MZ*tspan4a* (**c**) or MZ*tspan7* mutant (**e**) embryos. The arrows indicate migrasomes. Scale bars, 10 μm. **d**, Quantification of the number of migrasomes in WT and MZ*tspan4a*-mutant embryos. Data were pooled from three independent experiments. WT, $n = 64$ and MZ*tspan4a*, $n = 57$ embryos. **f**, Quantification of the number of migrasomes in WT and MZ*tspan7a*-mutant embryos. Data from three independent experiments were pooled. WT, $n = 68$ and MZ*tspan7*, $n = 60$ embryos. Data in **d**,**f** represent the mean ± s.e.m. *P* values were calculated using a two-tailed, unpaired *t*-test. **g**, The average speed of cell migration in WT, MZ*tspan4a* and MZ*tspan7* gastrulas was quantified. Light-sheet microscopy was used to acquire 4D images of gastrulas and the average migration speed was measured using Imaris software. $n = 4$ embryos per group pooled from two independent experiments. Data represent the mean ± s.e.m. *P* values were calculated using a two-tailed, unpaired *t*-test. The numerical source data for **d**,**f**,**g** are shown in Supplementary Table 3.

including left–right reversal of the liver primodium, intestinal bulb and pancreatic bud, bilateral duplication of the liver primodium and right-looping heart tubes (Fig. 3a). In both the MZ*tspan4a* and MZ*tspan7* mutants, approximately 20% of embryos showed abnormalities when probed with any single marker. We also checked the distribution of primordial germ cells using *nanos3* as a marker and found that about 20% of embryos had an abnormal distribution of the primordial germ cells (Fig. 3a). When all six markers were examined simultaneously, about 65% of the embryos of both mutants exhibited visible abnormalities in at least one organ (Fig. 3b,c and Supplementary Fig. 3f) and about 30% showed various laterality defects (Fig. 3d).

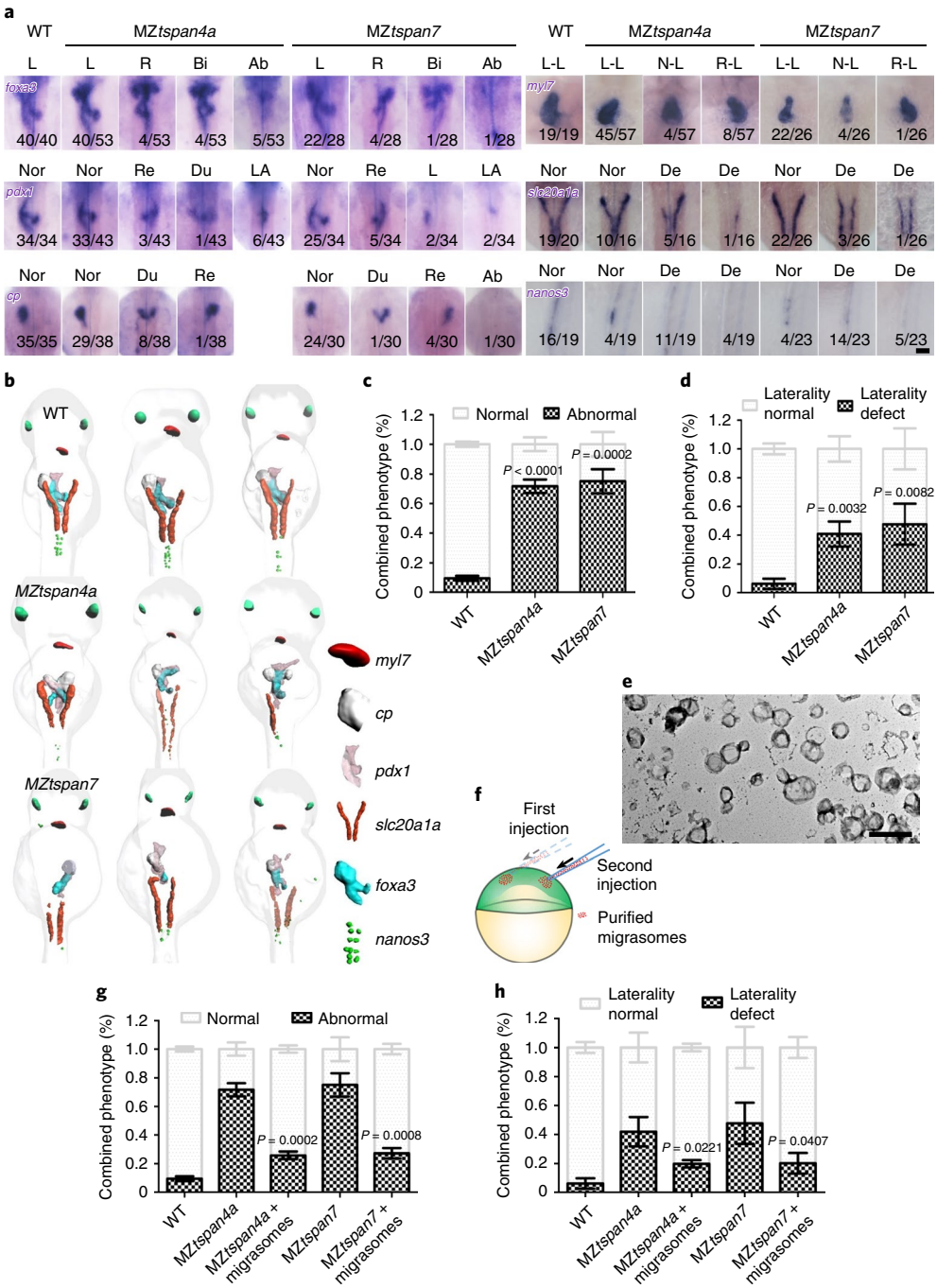

Fig. 3 | *tspan4a* and *tspan7* regulate zebrafish organ morphogenesis. a, Organ morphogenesis of the indicated embryos analysed by whole-mount ISH using probes for each organ. Scale bar, 100 µm. The ratio shown in each image represents 'the number of embryos with the indicated abnormality/the number of embryos analysed'. The experiment was performed once. L, left; R, right; Bi, bilateral; Ab, absent; Nor, normal; Re, reverse; Du, duplicate; LA, loss of asymmetry; L-L, left-looping; R-L, right-looping; N-L, no-looping; De, deformation. **b**, Embryos were simultaneously stained by FISH using combined probes for *myl7*, *slc20a1a*, *cp*, *foxa3*, *pdx1* and *nanos3*. The 3D images acquired by light-sheet microscopy are presented as 3D surface reconstructions processed by Imaris. Three embryos are shown for each group. **c**,**d**, Phenotypic categorization of the MZ*tspan4a* and MZ*tspan7* embryos in **b**. All deformed embryos, including those with left–right defects and impaired induction or development of tissue, were classed as 'abnormal' (**c**). Only embryos with a clear left–right phenotype were classed as having a 'laterality defect' (**d**). Embryos pooled from three independent experiments were used for quantification: WT, $n = 142$; MZ*tspan4a*, $n = 121$ and MZ*tspan7*, $n = 91$ embryos. *P* values are shown for comparisons to the WT. **e**, TEM image of purified migrasomes from zebrafish gastrulas. Scale bar, 1 µm. **f**, Diagram illustrating the procedure for migrasome injection at 30% epiboly. **g**,**h**, Phenotypic categorization of migrasome-injected embryos. The embryos were stained at 48 h.p.f. with the six primordial organ markers used in **b**. The embryos were quantified as described in **c**,**d**. Embryos pooled from three independent experiments were used for quantification: WT, $n = 142$; MZ*tspan4a*, $n = 121$; MZ*tspan4a* + migrasomes, $n = 83$; MZ*tspan7*, $n = 91$ and MZ*tspan7* + migrasomes, $n = 95$ embryos. *P* values are shown for comparisons of MZ*tspan4a* + migrasomes versus MZ*tspan4a* and MZ*tspan7* + migrasomes versus MZ*tspan7*. The WT, MZ*tspan4a* and MZ*tspan7* samples are the same as in **c**,**d**. Data in **c**,**d**,**g**,**h** represent the mean ± s.d. *P* values were calculated using a two-tailed, unpaired *t*-test. The experiments in **b**–**e**,**g**,**h** were performed three independent times with similar results. The numerical source data for **c**,**d**,**g**,**h** are shown in Supplementary Table 3.

Next, we carried out ISH of *spaw*, which is expressed at the left side at the late somite stage and is required for the establishment of left–right asymmetry of multiple organs[11–13]. We observed clear laterality defects, including right-sided and bilateral *spaw*, in approximately 50% of the MZ*tspan4a* and MZ*tspan7* mutants (Supplementary Fig. 4a).

Injection of exogenous migrasomes partially rescues organ morphogenesis in MZ*tspan4a* and MZ*tspan7* mutants. We then investigated whether the abnormal organ morphogenesis in MZ*tspan4a* and MZ*tspan7* mutants is caused by impaired migrasome formation or by migrasome-independent functions of *tspan4a* and *tspan7*. We reasoned that if the formation of defective migrasomes is the main cause of abnormal organ morphogenesis, we may be able to rescue the phenotype by adding migrasomes isolated from wild-type (WT) embryos. We purified migrasomes from WT gastrulas and injected them into MZ*tspan4a*- and MZ*tspan7*-mutant embryos before gastrulation (Fig. 3e,f). We found that only about 25% of migrasome-injected MZ*tspan4a* and MZ*tspan7* embryos had visible defects in organ morphogenesis—as revealed by the six markers—compared with approximately 65% of mutant embryos that were not injected with migrasomes (Fig. 3g,h). To rule out possible contamination of cell debris in the purified migrasomes, we tested whether samples from lysed cells—prepared in a similar way to the migrasomes—can rescue the phenotype. We found that samples from lysed cells (Supplementary Fig. 4b) could not rescue the phenotype (Supplementary Fig. 4c,d).

From these data, we concluded that facilitating migrasome formation is probably the main role of *tspan4a* and *tspan7* in organ morphogenesis.

Chemokines, morphogens and growth factors are enriched in migrasomes. We speculated that migrasomes may carry out their physiological function in vivo by releasing factors that can modulate the behaviours of surrounding cells. To identify factors in migrasomes that can affect organ morphogenesis, we carried out tandem-mass-tag (TMT) labelling followed by quantitative mass spectrometry. Purified migrasomes and cell bodies were isolated from approximately 20,000 embryos (Fig. 4a), and the quality of the isolated migrasomes was monitored by TEM (Fig. 4b) and western blotting using an antibody against Integrin β1b (Fig. 4c and Supplementary Fig. 4e). The samples were labelled with tags of different masses, combined and then analysed (Fig. 4d). We found that 2,680 proteins were enriched more than twofold in migrasomes and 3,710 proteins were depleted more than twofold in migrasomes (Fig. 4e). Thus, the protein composition of migrasomes is very different from cell bodies. Moreover, we found that Tspan7, Tspan4a and Integrin β1b were enriched more than twofold (Supplementary Table 1a and Supplementary Fig. 5a).

In the quantitative mass-spectrometry analysis, we found that migrasomes are enriched for a host of signalling molecules, including Tgfβ2, Il1β, PdgfD, Cxcl12b, Wnt11, Mydgf, DllD, Cxcl12a, Bmp1, Wnt8a, Chd, Bmp7a, Cxcl18a.1, Wnt5b, Lefty1 and Bmp2 (Supplementary Table 1b). We noticed that the chemokines Cxcl12a and Cxcl12b were enriched inside embryonic migrasomes. Cxcl12 plays an important role in organ morphogenesis and deficiency of *cxcl12* in zebrafish causes organ-morphogenesis defects[14] that are somewhat similar to the phenotypes we observed in MZ*tspan4a* and MZ*tspan7* mutants. For this reason, we focused our investigation on Cxcl12.

To confirm the enrichment of Cxcl12 in migrasomes, we generated antibody to zebrafish Cxcl12. We successfully generated a specific antibody against zebrafish Cxcl12a (Supplementary Fig. 5b,c). Immunostaining and western blotting using this antibody confirmed that endogenous Cxcl12a was indeed highly enriched in migrasomes in vivo (Fig. 4f,g and Supplementary Fig. 5d) and in zebrafish embryonic cells cultured in vitro (Fig. 4h).

The Cxcl12a–Cxcr4b signalling axis is required for organ morphogenesis. The enrichment of Cxcl12a in migrasomes raises the possibility that the Cxcl12a (ligand)–Cxcr4b (receptor) signalling axis is required for organ morphogenesis. To directly test this hypothesis, we first used ISH to verify that Cxcl12a and Cxcr4b are indeed expressed in gastrulas (Supplementary Fig. 5e). We then generated *cxcl12a*$^{-/-}$ fish and acquired MZ*cxcr4b* fish. We found that organ morphogenesis, including laterality, is impaired in both mutants (Supplementary Fig. 5f,g).

We injected the purified migrasomes from WT gastrulas into Cxcl12a morphant embryos to test whether migrasomes can deliver Cxcl12a for signalling. We found that these migrasomes potently rescued organ morphogenesis and the laterality defect (Supplementary Fig. 5h,i). From these data, we conclude that migrasomes can work as a source of Cxcl12a during gastrulation.

Kupffer's vesicles require *tspan4a* and *tspan7* to form. The morphogenesis defects in MZ*tspan4a* and MZ*tspan7* mutants are quite complex and may arise from multiple underlying mechanisms. We focused our in-depth analysis on laterality defects, as the mechanisms underlying laterality are relatively well established. It is known that the Kupffer's vesicle (KV) plays an essential role in establishing the left–right body axis in teleost fish[15]. We found that the formation of KV was impaired in both MZ*tspan4a* and MZ*tspan7* mutants, manifesting as a smaller KV with fewer cilia (Fig. 5a–c). It is worth noting that the severity of the KV abnormality varied considerably among individual mutant embryos, ranging from a tiny KV to a mild reduction in KV size. This probably explains the considerable variation in the severity of morphogenetic organ defects observed at 48 h.p.f. To directly test the role of migrasomes in KV formation, we carried out a rescue experiment. We found that injection of purified migrasomes from WT embryos rescued the KV size and the number of cilia in both MZ*tspan4a* and MZ*tspan7* mutants (Fig. 5d–f).

Finally, we investigated whether the Cxcl12a–Cxcr4b signalling axis is required for KV formation. We found that KV formation was impaired in both the *cxcl12a* and *cxcr4b* mutants (Fig. 5g–i), which suggests that the Cxcl12a–Cxcr4b signalling axis is indeed required for KV formation. Together, these data suggest that migrasomes regulate KV formation by providing Cxcl12a for signalling, which in turn modulates laterality.

***tspan4a* and *tspan7* are required for the clustering of DFCs on the embryonic shield during gastrulation.** In zebrafish, the KV is formed by a cluster of cells named dorsal forerunner cells (DFCs)[16]. During gastrulation, DFCs migrate to the leading edge of the embryonic shield. In contrast to other blastodermal cells in the embryonic shield, DFCs do not involute; instead, they remain tightly clustered during epiboly[16]. The impaired KV formation prompted us to check whether the migration or clustering of DFCs is affected in the MZ*tspan4a* and MZ*tspan7* mutants. We found that DFC clustering was abnormal in both the MZ*tspan4a* and MZ*tspan7* mutants, a significant percentage of which had smaller or scattered DFCs clusters (Fig. 6a).

If *tspan4a* and *tspan7* affect the migration or clustering of DFCs by regulating migrasome formation, *tspan4a* and *tspan7* should carry out their function in a cell non-autonomous manner. To test this hypothesis, we carried out DFC-transplantation experiments. As *sox17* is expressed at high levels in DFCs, we transplanted WT DFCs from *Tg(sox17:GFP)* embryos to the DFC region of WT, MZ*tspan4a* and MZ*tspan7* embryos at 6–7 h.p.f. (Fig. 6b), and took 4D images using light-sheet microscopy from 7–8 h.p.f. to the early somite stage (12 h.p.f.). We found that the transplanted DFCs migrated as a tight cluster on the leading edge of the embryonic shield during gastrulation in WT host embryos, whereas in the MZ*tspan4a*- and MZ*tspan7*-mutant hosts, the transplanted DFCs failed to stay together and scattered during migration (Fig. 6c,d

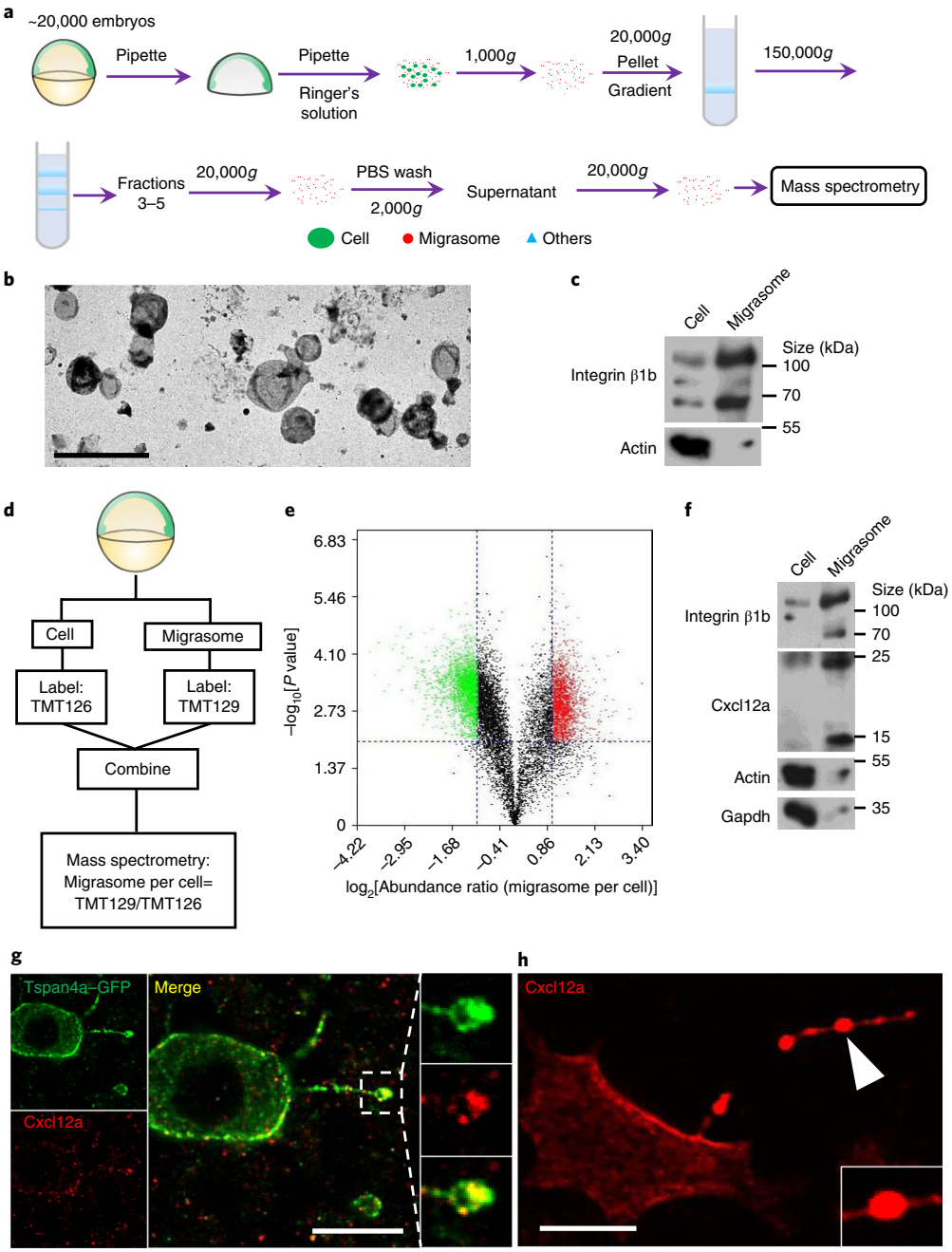

Fig. 4 | Chemokines, morphogens and growth factors are enriched in migrasomes. a, Diagram of the migrasome purification procedure. **b**, TEM image of purified migrasomes from zebrafish gastrulas. **c**, Verification of purified migrasomes by western blot analysis using an anti-Integrin β1b antibody. **d**, Diagram of the TMT-labelling procedure. Proteins from the cell bodies and migrasomes were labelled using TMTs with different masses. **e**, Volcano plot showing the mass-spectrometry-based quantification of TMT-labelled proteins. The red dots represent a migrasome:cell abundance ≥ 2, $P < 0.01$; the green dots represent a migrasome:cell abundance < 0.5, $P < 0.01$. $n = 3$ biologically independent experiments. *P* values were calculated using a two-tailed, two-sample unequal variance *t*-test using Excel. **f**, Enrichment of Cxcl12a in isolated migrasomes. The lysates of the cell bodies and migrasomes were normalized to the total protein concentration. Integrin β1b was used as the positive control, and Actin and Gapdh were used as the negative controls. **g**, Immunostaining of endogenous Cxcl12a in a zebrafish gastrula. Embryos at the 16-cell stage were injected with *tspan4a–GFP* mRNA and gastrulas were co-stained with antibodies to detect GFP and endogenous Cxcl12a. **h**, Endogenous Cxcl12a is enriched in migrasomes in zebrafish primary cells cultured in vitro. The experiments in **c**,**f** were performed twice. The experiments in **b**,**g**,**h** were performed three independent times with similar results. The unprocessed blots for **c**,**f** are shown in Supplementary Fig. 8. Scale bars, 5 μm (**a**) and 10 μm (**g**,**h**).

and Supplementary Video 6). These data indicate that *tspan4a* and *tspan7* function in a cell non-autonomous manner. Together, these results indicate that *tspan4a* and *tspan7* are required for the clustering of DFCs during gastrulation through a cell non-autonomous mechanism.

Migrasomes are enriched in a cavity underneath the embryonic shield. The enrichment of Cxcl12a in migrasomes suggests the possibility that migrasomes may serve as regional chemoattractants that attract and hold DFCs at the front of the embryonic shield. If so, we would expect migrasomes to be enriched around the embryonic

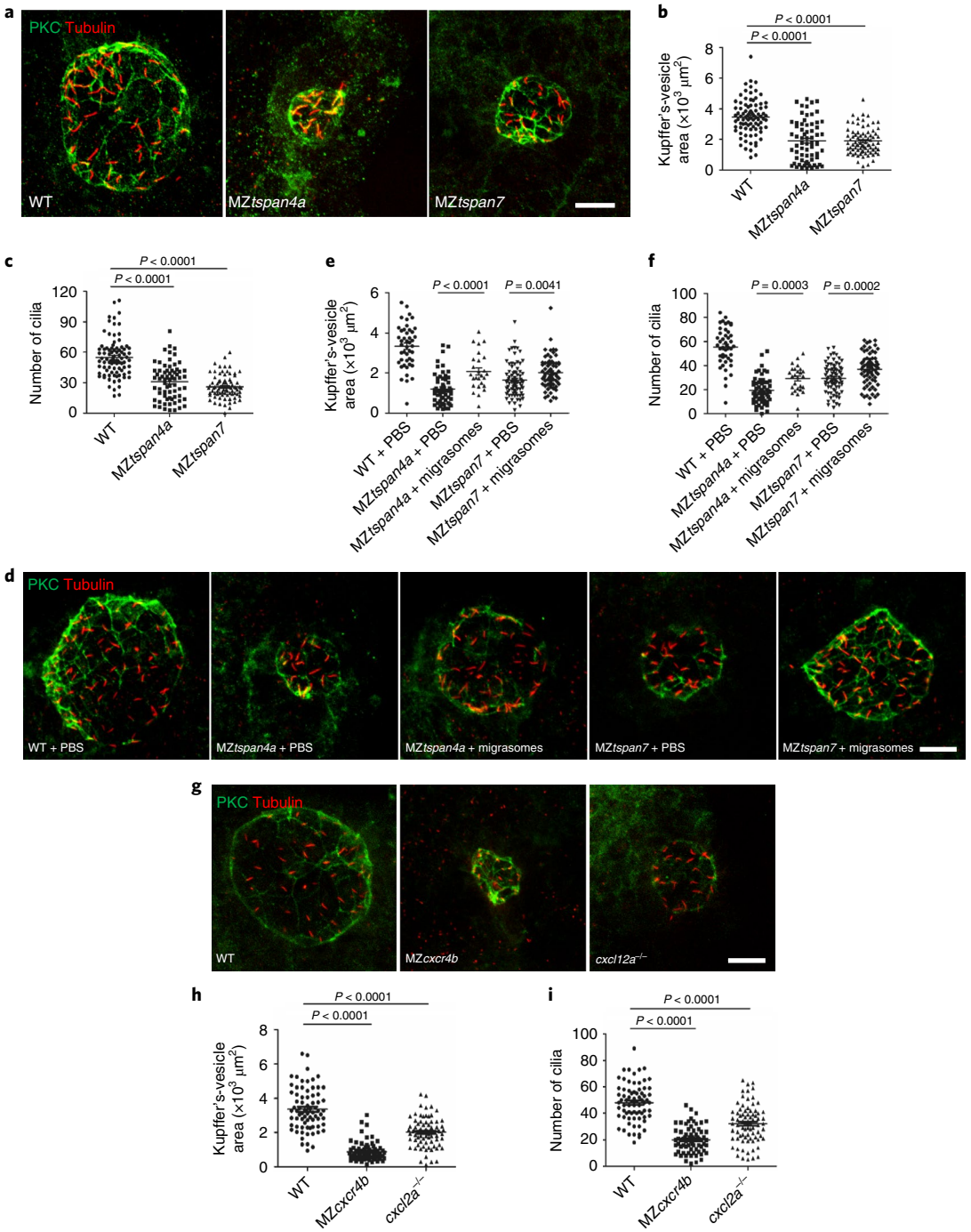

Fig. 5 | Migrasomes are required for formation of the KV. a, WT, and MZ*tspan4a*- and MZ*tspan7*-mutant embryos were analysed at the six-somite stage for KV formation by immunostaining with anti-PKC and anti-Tubulin antibodies, and *z*-stack images were acquired by confocal microscopy. **b**,**c**. Quantification of the KV size and number of cilia for the experiments in **a**. Data from three independent experiments were pooled. WT, $n=86$; MZ*tspan4a*, $n=67$ and MZ*tspan7*, $n=79$ embryos. **d**, WT, MZ*tspan4a* and MZ*tspan7* embryos were injected with PBS or migrasomes, as indicated, and then analysed at the six-somite stage for KV formation by immunostaining with anti-PKC and anti-Tubulin antibodies. The *z*-stack images were acquired by confocal microscopy. **e**,**f**. Quantification of the KV size and cilium number in WT, MZ*tspan4a* and MZ*tspan7* embryos injected with PBS or migrasomes as in **d**. Data from three independent experiments were pooled. WT + PBS, $n=45$; MZ*tspan4a* + PBS, $n=58$; MZ*tspan4a* + migrasomes, $n=26$; MZ*tspan7* + PBS, $n=79$ and MZ*tspan7* + migrasomes, $n=72$ embryos. **g**, WT, and *cxcr4b*- and *cxcl12a*-mutant embryos were analysed at the six-somite stage for KV formation by immunostaining with anti-PKC and anti-Tubulin antibodies, and *z*-stack images were acquired by confocal microscopy. **h**,**i**, Quantification of the KV size and number of cilia in the embryos from **g**. Data from three independent experiments were pooled. WT, $n=73$; MZ*cxcr4b*, $n=71$ and *cxcl12a*$^{-/-}$, $n=77$ embryos. Data in **b**,**c**,**e**,**f**,**h**,**i** represent the mean ± s.e.m. *P* values were calculated using a two-tailed, unpaired *t*-test. The numerical source data for **b**,**c**,**e**,**f**,**h**,**i** are shown in Supplementary Table 3. Scale bars, 20 µm.

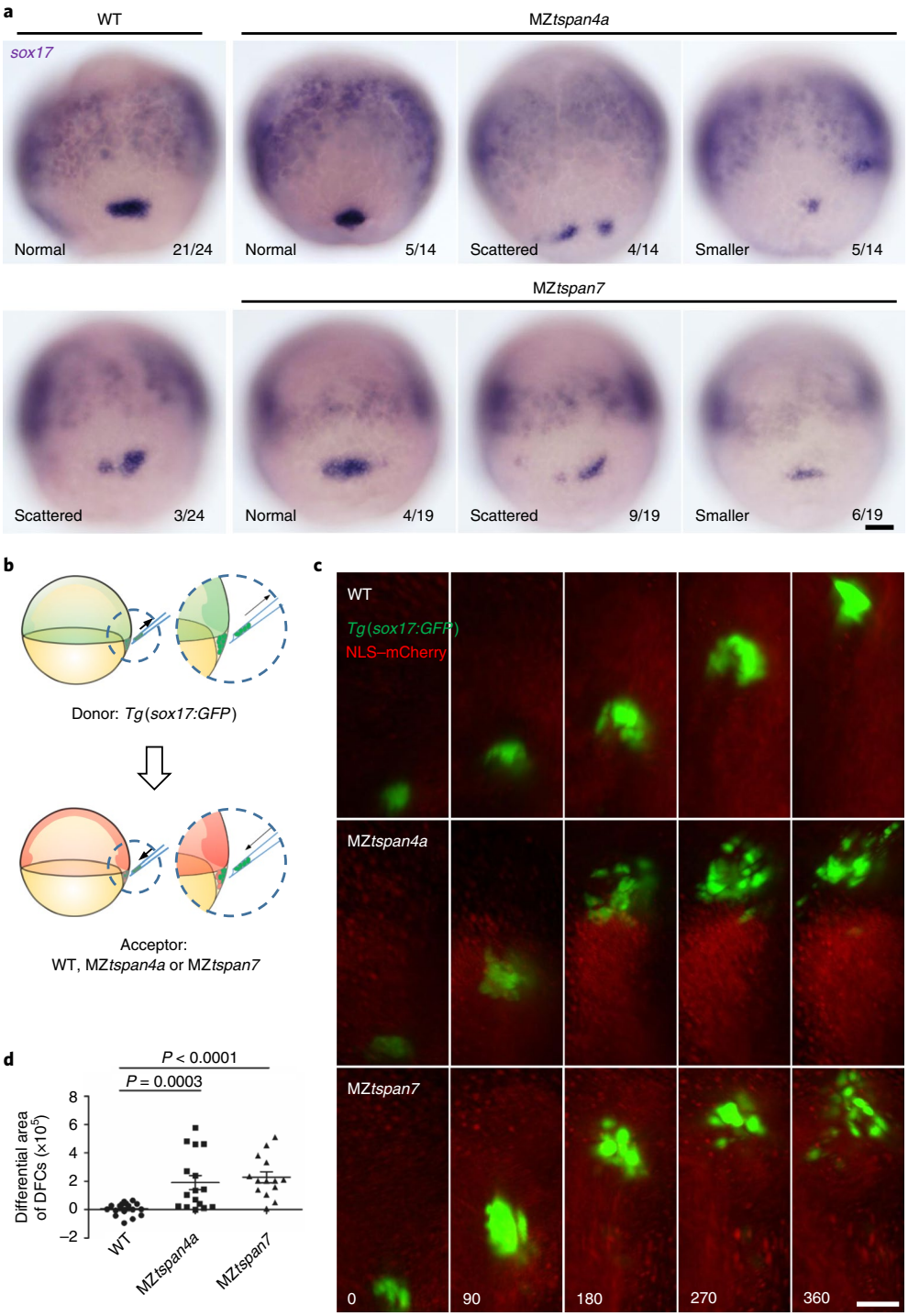

Fig. 6 | *tspan4a* and *tspan7* are required for the clustering of DFCs on the embryonic shield during gastrulation. a, In situ hybridization of *sox17*. MZ*tspan4a* and MZ*tspan7* mutants show obvious defects in DFC positioning at the 70% epiboly stage. The ratio shown in each image represents 'the number of embryos with the indicated abnormality/the number of embryos analysed'. The experiment was performed once. **b**, Diagram illustrating the procedure for DFC transplantation. DFCs (green) from WT *Tg(sox17:GFP)* embryos were transplanted into the DFC region of WT, and MZ*tspan4a*- or MZ*tspan7*-mutant (red) embryos at the shield stage. **c**, Light-sheet microscopy was used to acquire 4D images to monitor the migration of the transplanted DFCs. Times (in min) are indicated on the lower images. **d**, Quantification of DFC scattering. The area occupied by DFCs was analysed in the time-lapse images from **c**. The differential area is defined as the area occupied by DFCs in the end frame minus the area occupied by DFCs in the start frame ($A_d = A_e - A_s$). Data from three independent experiments were pooled. WT, $n = 17$; MZ*tspan4a*, $n = 16$ and MZ*tspan7*, $n = 14$ embryos. Data represent the mean ± s.e.m. *P* values were calculated using a two-tailed, unpaired *t*-test. The numerical source data for **d** are shown in Supplementary Table 3. Scale bars, 100 μm.

shield. As shown in Fig. 1j, migrasomes are enriched in the cavities of zebrafish gastrulas, implying that a migrasome-enriched cavity may exist beneath DFCs. To test this idea, we labelled cavities in zebrafish gastrulas by injecting high-molecular-weight fluorescently labelled dextrans into *Tg(sox17:GFP)* embryos, which express GFP in DFCs. Rapid three-dimensional (3D) imaging revealed that

the fluorescently labelled dextrans accumulated in a defined area underneath the DFCs (Fig. 7a and Supplementary Video 7a), indicating that there is a cavity beneath the DFCs. A more detailed analysis revealed that this cavity was present throughout the entire gastrulation process in every gastrula examined and the position of DFCs relative to the cavity did not change during gastrulation. We named this cavity the embryonic shield cavity.

Next, we checked whether migrasomes are present in the embryonic shield cavity by injecting *tspan4a–mCherry* mRNA into blastomeres of *Tg(sox17:GFP)* embryos at the eight-cell stage and observing the embryonic shield cavity by light-sheet microscopy. We found that migrasomes were highly enriched in the embryonic shield cavity (Fig. 7b and Supplementary Video 7b), whereas the accumulation of migrasomes in the embryonic shield cavity was markedly reduced in MZ*tspan4a* or MZ*tspan7* embryos (Supplementary Fig. 6a,b and Supplementary Video 8). We also checked whether injected migrasomes (Fig. 3e,f) accumulated in the embryonic shield cavity. We stained the purified migrasomes with CM-DiI and then injected them into *Tg(sox17:GFP)* embryos at the 50% epiboly stage. We found that the injected migrasomes homed to the correct region and accumulated in the embryonic shield cavity (Fig. 7c and Supplementary Video 7c). Based on these data, we conclude that migrasomes accumulate in the embryonic shield cavity (Fig. 7d). The accumulation of exogenous migrasomes at the right place probably explains why the rescue experiment was successful.

Migrasomes are chemoattractants for DFCs. To directly test whether migrasomes are chemoattractants for DFCs, we designed an in vivo chemoattraction assay. First, we purified migrasomes from zebrafish gastrulas and then embedded them with fluorescent beads in 1% low-melting-point agarose. Next, we injected control and migrasome-containing agarose into the ventral surface of a *Tg(sox17:GFP)* gastrula in which the endodermal cells and DFCs were labelled (Fig. 7e). As expected, endodermal cells and DFCs stayed on the dorsal side of gastrulas injected with control agarose; however, in gastrulas injected with agarose-embedded migrasomes, a group of endodermal cells and DFCs were attracted to the ventral side of embryos and eventually surrounded the agarose (Fig. 7f,g and Supplementary Video 9).

Cxcl12 is enriched in migrasomes and is known to play important roles in embryonic development[8]. We speculated that Cxcl12 may be a main chemoattractant in migrasomes. To test this hypothesis, we combined *cxcl12a* and *cxcl12b* morpholino oligonucleotides, isolated migrasomes from *cxcl12a/b* morphants at gastrulation stage, embedded the migrasomes in agarose and injected them into host embryos. The results showed that migrasomes from *cxcl12a/b* morphants have a reduced ability to attract endodermal cells and DFCs (Fig. 7f,g and Supplementary Video 9). This indicates that Cxcl12a/b are probably the main chemoattractants in migrasomes.

If Cxcl12a/b are the main chemoattractants in migrasomes for DFCs, Cxcr4b/a should be expressed in DFCs. We found that both Cxcr4b and Cxcr4a are indeed expressed in DFCs (Fig. 7h and Supplementary Fig. 7a). In addition, the migration and clustering of DFCs is impaired in *cxcr4b* mutants (Supplementary Fig. 7b), which suggests that Cxcl12a/b are the main chemoattractants for DFCs. Together, these data imply that migrasomes are chemoattractants for DFCs.

Discussion

In this study, we describe our effort to establish an in vivo model to study migrasomes and migracytosis. We document the formation of vesicles on long cellular projections in zebrafish gastrulas. The morphology, biogenesis and molecular composition of these vesicles indicate that they are migrasomes. We cannot of course rule out the possibility that other types of extracellular vesicles may also be generated during gastrulation. However, the markedly reduced vesicle numbers in *itgb1b*$^{-/-}$ gastrulas argues that the majority of PH-positive vesicles formed during gastrulation are migrasomes, as migrasome formation is dependent on Integrin β1. At present, we do not know whether distinct cell types differ in their capacity to generate migrasomes or whether migrasomes from different cell types or from different areas of the embryo—at different developmental stages—have different compositions with distinct roles. Future investigations using transgenic fish with cell-type-specific expression of the PH domain and fish with cell-type-specific knockout of *tspan4a* and *tspan7* are required to answer these important questions.

We generated *tspan4a* and *tspan7* knockout fish and found that migrasomes are significantly less abundant, but not completely eliminated, in MZ mutants. It is probable that other tetraspanins may compensate for the deficiency of Tspan4a or Tspan7, as we recently found that overexpressing 14 out of 33 known tetraspanins can induce migrasome formation in mammalian cells[17]. Using these models, we showed that migrasomes play important roles in early embryonic development. We found that organ morphogenesis was impaired in MZ*tspan4a* and MZ*tspan7* mutants; importantly, these phenotypes can be largely rescued by the injection of purified migrasomes before gastrulation. Thus, impaired organ morphogenesis in mutants probably results directly from defective migrasome formation rather than from the migrasome-independent functions of Tspan4 and Tspan7. Our mechanistic study revealed that the DFCs, which give rise to the KV, fail to cluster at the leading edge of the embryonic shield in mutant embryos; instead, the DFCs are dispersed, which results in defective KV formation and probably explains the morphogenesis phenotypes related to laterality.

Our quantitative mass-spectometry analysis showed that a collection of signalling molecules—including chemokines, morphogens, growth factors and cytokines—are enriched in migrasomes. Many of these signalling molecules are known for their roles in embryonic development and the enrichment of the these signalling molecules in migrasomes suggests that migrasomes may have multiple roles in embryonic development. If migrasomes do indeed have multiple roles in the regulation of embryonic development, why is the phenotype largely restricted to organ morphogenesis? We think there are likely to be multiple possible explanations for this discrepancy. First, given that our analysis was focused on organ morphogenesis, it is very probable that there were other abnormalities that were not revealed by our study. Second, knockout of *tspan4a* and *tspan7* only partially blocks migrasome formation; thus, it is possible that the remaining migrasomes in mutant embryos can provide sufficient relevant cues for embryonic development, while signalling molecules required for proper organ morphogenesis (like Cxcl12a) remain under the thresholds.

We found that Cxcl12a, and potentially Cxcl12b, are enriched in migrasomes and migrasomes are enriched in a large cavity underneath the embryonic shield (the embryonic shield cavity). The fact that agarose with embedded migrasomes is capable of attracting and holding *sox17:GFP*-positive cells suggests that migrasomes are chemoattractants for *sox17:GFP*-positive cells. Based on these data, we propose that the migrasomes enriched in the embryonic shield cavity hold DFCs at the edge of the embryonic shield through Cxcl12-mediated chemoattraction.

It is well established that the Cxcl12b–Cxcr4a signalling axis plays an important role in organ morphogenesis. Organ morphogenesis defects similar to those in MZ*tspan4a* and MZ*tspan7* mutants have been shown in *cxcl12b/a* morphant fish[14]. In our study, we demonstrated that the Cxcl12a–Cxcr4b signalling axis is also required for organ morphogenesis. As both Cxcl12a and Cxcl12b are enriched in migrasomes, it is very probable that migrasomes regulate organ morphogenesis by delivering Cxcl12a and Cxcl12b for signalling.

How are migrasomes enriched in the embryonic shield cavity? Given the degree of enrichment, it is unlikely that they are generated

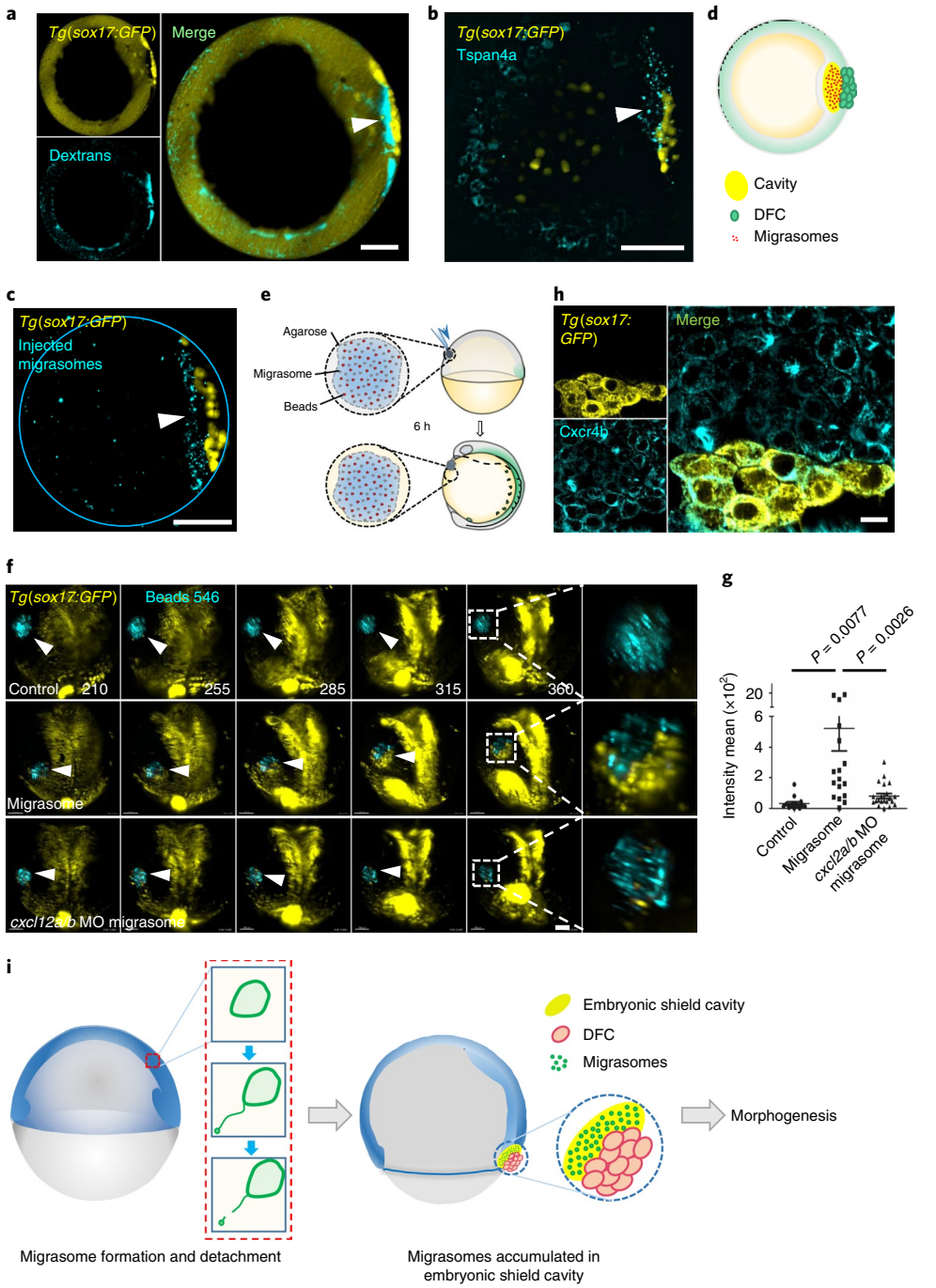

Fig. 7 | Migrasomes are chemoattractants for DFCs. a, The embryonic shield cavity, revealed by injection of fluorescently labelled dextrans that were injected into *Tg(sox17:GFP)* embryos at the 50% epiboly stage and imaged 1 h later by light-sheet microscopy. The arrow indicates the embryonic shield cavity. **b**, Single blastomeres of *Tg(sox17:GFP)* embryos at the eight-cell stage were injected with *tspan4a–GFP* mRNA and the embryos were imaged for migrasomes at the shield stage using a light-sheet microscope. The arrow indicates migrasomes enriched in the embryonic shield cavity under the DFCs (yellow). **c**, Purified migrasomes were stained with CM-DiI and injected into *Tg(sox17:GFP)* embryos at 50% epiboly. The embryos were imaged 1 h later by light-sheet microscopy. The arrow indicates migrasomes enriched in the embryonic shield cavity under the DFCs (yellow). The experiments in **a**–**c** were performed twice. **d**, Diagram of the embryonic shield cavity as described in **a**–**c**. **e**, Diagram of the procedure for the in vivo chemoattraction assay. **f**, PBS (upper) and purified migrasomes from WT embryos (middle) or *cxcl12a/b* morphants (lower) were embedded in 1% low-melting-point agarose containing fluorescent beads (cyan) and injected into the ventral side of *Tg(sox17:GFP)* embryos at the shield stage. Light-sheet microscopy was used to acquire 3D time-lapse images. The DFCs are labelled in yellow. The right-hand images show enlarged images of the injected agarose after 360 min. The arrows indicate the injected beads. Times (in min) are indicated on the upper images. **g**, The images from **f** were quantified for the fluorescence intensity of GFP-positive endodermal cells and DFCs (yellow) that accumulated around the agarose. Data from three independent experiments were pooled. Control, $n = 14$; migrasomes, $n = 19$ and *cxcl12a/b* morpholino oligonucleotide (MO) migrasomes, $n = 22$ embryos. Data represent the mean ± s.e.m. *P* values were calculated using a two-tailed, unpaired *t*-test. **h**, *Tg(sox17:GFP)* transgenic zebrafish gastrulas were stained with antibodies against GFP and endogenous Cxcr4b. The experiments were performed twice independently with similar results. **i**, Model for the role of migrasomes in morphogenesis. The numerical source data for **g** are shown in Supplementary Table 3. Scale bars, 100 μm (**a**–**c**,**f**) and 10 μm (**h**).

locally. One possibility is that migrasomes are generated elsewhere by migrating cells and after breaking from the retraction fibres they are 'washed' to the embryonic shield cavity by moving cells (Fig. 7i). The fact that injected exogenous migrasomes end up being enriched in the embryonic shield cavity supports this hypothesis.

It is well established that chemical gradients formed by soluble ligands is a main signalling mechanism to coordinate embryonic development[1]. We would like to propose that migracytosis is a new type of signalling mechanism for development, in which chemical signals are packaged into a membrane-bound compartment and released as a unit. These signal units may be redistributed in embryos by embryonic fluid flow or other mechanisms, resulting in the establishment of localized regional signalling centres on a restricted area of the embryo, such as the embryonic shield cavity. We demonstrated that signalling molecules—including chemokines, morphogens, cytokines and growth factors—are enriched inside migrasomes, which suggests that a combination of ligands can be loaded into a single migrasome, transported to a defined location and released from the migrasome in a synchronized manner. In this way, combinatory signalling with defined spatial and potentially temporal restriction can be established, thus generating the complex information that is required for encoding the organization of embryonic development.

Online content

Any methods, additional references, Nature Research reporting summaries, source data, statements of code and data availability and associated accession codes are available at https://doi.org/10.1038/s41556-019-0358-6.

Received: 15 April 2018; Accepted: 10 June 2019;
Published online: 1 August 2019

References

1. Rogers, K. W. & Schier, A. F. Morphogen gradients: from generation to interpretation. *Ann. Rev. Cell Dev. Biol.* **27**, 377–407 (2011).
2. Ma, L. et al. Discovery of the migrasome, an organelle mediating release of cytoplasmic contents during cell migration. *Cell Res.* **25**, 24–38 (2015).
3. Grunwald, D. J. & Eisen, J. S. Headwaters of the zebrafish–emergence of a new model vertebrate. *Nat. Rev. Genet.* **3**, 717–724 (2002).
4. Lieschke, G. J. & Currie, P. D. Animal models of human disease: zebrafish swim into view. *Nat. Rev. Genet.* **8**, 353–367 (2007).
5. Keller, P. J., Schmidt, A. D., Wittbrodt, J. & Stelzer, E. H. Reconstruction of zebrafish early embryonic development by scanned light sheet microscopy. *Science* **322**, 1065–1069 (2008).
6. Wu, D. et al. Pairing of integrins with ECM proteins determines migrasome formation. *Cell Res.* **27**, 1397–1400 (2017).
7. Stoolman, L. M. Adhesion molecules controlling lymphocyte migration. *Cell* **56**, 907–910 (1989).
8. Nair, S. & Schilling, T. F. Chemokine signaling controls endodermal migration during zebrafish gastrulation. *Science* **322**, 89–92 (2008).
9. Charrin, S., Jouannet, S., Boucheix, C. & Rubinstein, E. Tetraspanins at a glance. *J. Cell Sci.* **127**, 3641–3648 (2014).
10. Rubinstein, E. The complexity of tetraspanins. *Biochem. Soc. Trans.* **39**, 501–505 (2011).
11. Tessadori, F. et al. Nodal signaling range is regulated by proprotein convertase-mediated maturation. *Dev. Cell* **32**, 631–639 (2015).
12. Bisgrove, B. W., Snarr, B. S., Emrazian, A. & Yost, H. J. Polaris and Polycystin-2 in dorsal forerunner cells and Kupffer's vesicle are required for specification of the zebrafish left-right axis. *Dev. Biol.* **287**, 274–288 (2005).
13. Montague, T. G., Gagnon, J. A. & Schier, A. F. Conserved regulation of Nodal-mediated left-right patterning in zebrafish and mouse. *Development* **145**, dev171090 (2018).
14. Mizoguchi, T., Verkade, H., Heath, J. K., Kuroiwa, A. & Kikuchi, Y. Sdf1/Cxcr4 signaling controls the dorsal migration of endodermal cells during zebrafish gastrulation. *Development* **135**, 2521–2529 (2008).
15. Essner, J. J., Amack, J. D., Nyholm, M. K., Harris, E. B. & Yost, J. Kupffer's vesicle is a ciliated organ of asymmetry in the zebrafish embryo that initiates left-right development of the brain, heart and gut. *Development* **132**, 1247–1260 (2005).
16. Oteiza, P., Koppen, M., Concha, M. L. & Heisenberg, C. P. Origin and shaping of the laterality organ in zebrafish. *Development* **135**, 2807–2813 (2008).
17. Huang, Y. et al. Migrasome formation is mediated by assembly of micron-scale tetraspanin macrodomains. *Nat. Cell Biol.* https://doi.org/10.1038/s41556-019-0367-5 (2019).

Acknowledgements

We are grateful to the members of the Meng and Yu groups for their helpful discussions. This research was supported by the Ministry of Science and Technology of the People's Republic of China (grant nos 2017YFA0503404 and 2016YFA0500202 to L.Y. and 31590832 to A.M.), the National Natural Science Foundation of China (grant nos 31430053 and 31621063), the Natural Science Foundation of China International Cooperation and Exchange Program (grant no. 31561143002), and the Independent Research of Tsinghua University (grant no. 20161080135) to L.Y. We thank the State Key Laboratory of Biomembrane and Membrane Biotechnology for confocal microscopy imaging and facility support. We thank the Beijing Frontier Research Center for Biological Structure for facility support. We would like to acknowledge the assistance of the Imaging Core Facility, Technology Center for Protein Sciences, Tsinghua University for assistance with spinning disk microscopy and Imaris analysis. We thank the Protein Chemistry Facility at the Center for Biomedical Analysis of Tsinghua University for mass-spectrometry sample analysis. We thank the Core Facility of the Center of Biomedical Analysis, Tsinghua University for assistance with light-sheet imaging. We thank the National Center for Protein Sciences at Peking University for assistance with light-sheet imaging. We thank the F. Liu lab (Institute of Zoology, Chinese Academy of Sciences) for sharing the *cxcr4b* mutant with us.

Author contributions

L.Y. and A.M. conceived the experiments, wrote the paper and supervised the project. D.J. and Z.J. carried out the experiments. D.L., X.W. and H.L. helped to purify migrasomes and construct plasmids. J.Z. and Y.M. contributed to the mutant-zebrafish verification. D.W. and Y.H. contributed the staining of Integrin β1 in the mammalian cell line. Y.L. carried out the TEM sample preparation. Y.C. and H.D. contributed to the TMT-labelled mass spectrometry. Q.W. and J.X. provided the *itgb1b* mutant. All authors discussed the manuscript, commented on the project and contributed to the preparation of the paper.

Competing interests

The authors declare no competing interests.

Additional information

Supplementary information is available for this paper at https://doi.org/10.1038/s41556-019-0358-6.

Reprints and permissions information is available at www.nature.com/reprints.

Correspondence and requests for materials should be addressed to A.M. or L.Y.

Publisher's note: Springer Nature remains neutral with regard to jurisdictional claims in published maps and institutional affiliations.

Methods

Experimental model and subject details. All WT zebrafish used in this study were from the Tuebingen (Tu) strain. The *Tg(sox17:GFP)*^{s870} transgenic line was described previously[18]. The *itgb1b* mutant was a gift from J. Xiong. The *Cxcr4b* mutant was a gift from F. Liu. All adult zebrafish used to produce eggs in this study were kept in a water-circulating system at 28.5 °C. Fertilized eggs were raised at 28.5 °C in Holtfreter's solution (0.059 M NaCl, 0.00067 M KCl, 0.00076 M $CaCl_2$ and 0.0024 M $NaHCO_3$). The use of all zebrafish adults and embryos was conducted according to the guidelines from the Animal Care and Use Committee of Tsinghua University.

RNA sequencing. About 50 wild-type zebrafish gastrulas at 60% epiboly stage were collected to check the expression levels of different *tspan* genes in zebrafish gastrulas. These embryos were lysed in 600 µl RLT solution (QIAGEN RNeasy mini kit, cat no. 74104) after the removal of the chorion. The lysis was kept at −80 °C until sequencing. RNA sequencing was analysed by the BGI company. Note, we used 600 µl RLT solution containing 24 µl dithiothreitol solution (7.71 g dithiothreitol ($C_4H_{10}O_2S_2$, Beijing Dingguo Changsheng Biotechnology Co., Ltd, CD116) in 50 ml 0.01 M sodium acetate, pH 5.2).

Generation of the *itgb1b* mutant using a TALENs system. TALENs were assembled according to Huang and colleagues[19]. TALEN mRNAs were transcribed using a T7 mMACHINE kit (Ambion). Embryos at the single-cell stage were injected with approximately 2 nl of the transcribed mRNA (50 ng µl^{-1}). Mutant lines with a 56-base pair deletion and a 1-base pair insertion were kept.

Generation of *tspan4a*, *tspan7* and *cxcl12a* mutant lines by CRISPR–Cas9. To generate the F_0 generation of mutants, 100 pg of each of the guide RNAs (target sequence in Supplementary Table 2) were co-injected with 300 pg *Cas9* mRNA into Tu embryos at the single-cell stage. Tail-fin clips from the F_1 generation were genotyped by PCR and sequencing using the primers listed in Supplementary Table 2. Mutant lines with out-of-frame insertions or deletions were kept.

Morpholinos and mRNA injection. Antisense morpholino oligonucleotides were synthesized by Gene Tools, LLC (sequences in Supplementary Table 2). All morpholino oligonucleotides were injected into Tu embryos at the single-cell stage. The embryos used in the transplantation assays were injected with either 100 pg *nuclear localization signal* (*nls*)*–mCherry* mRNA or 100 pg *nls–GFP* mRNA at the single-cell stage.

Whole-mount RNA ISH. The templates for all of the probes were amplified by PCR from complimentary DNA of embryos at specific stages. The sequences of the primers are listed in Supplementary Table 2. The *sox17* probe was previously reported[18]. The dorsal–ventral marker probes *chd*, *gsc*, *bmp4* and *eve1* were from a previous study[20]. Whole-mount ISH and synthesis of digoxigenin/fluorescein-labelled antisense RNA probes were performed as described previously[21]. Whole-mount double fluorescent ISH (FISH) was performed as described previously[22].

Measurement of convergence and extension movement. To measure the convergence and extension movement of the *MZtspan4a* and *MZtspan7* mutants, the embryos were fixed with 4% paraformaldehyde at the bud stage (10 h.p.f.). Wild-type Tu embryos were used as controls. All embryos were analysed by ISH using the *ntl* and *dlx3b* probes. The convergence movement distance was measured from the vegetal pole to the dorsal region where *ntl* expression ceased. The extension movement distance was measured between the left and right boundaries of *dlx3b* expression. The *ntl* and *dlx3b* probes were from a previous study[23].

Measurement of epiboly speed. Wild-type, *MZtspan4a* and *MZtspan7* embryos were incubated at 28.5 °C and photographs were taken at 6.5 and 9.0 h.p.f. The distance from the animal pole to the margin was measured at each time point and the following calculation was applied: epiboly speed = (distance at 9.0 h.p.f. − distance at 6.5 h.p.f.)/2.5 h.

Quantitative proteomics analysis. For the quantitative proteomics analysis, cells and migrasomes were lysed using lysis buffer containing 8 M urea and protease inhibitor (BioTools) in PBS. Equal amounts of protein were reduced, alkylated and digested by trypsin, and then desalted and labelled with different TMT reagents (Thermo, Pierce Biotechnology). The TMT-labelled peptides were mixed and desalted using Sep-Pak C18 cartridges. The tryptic peptides were separated into 24 fractions with high-pH RPLC (XBridge BEH300 C18 5 µm, 300 Å, 250 mm × 4.6 mm inner diameter; Waters; mobile phases A (2% acetonitrile, pH 10.0) and B (98% acetonitrile, pH 10.0)).

Cells and migrasomes were lysed using lysis buffer containing 4% SDS and protease inhibitor (BioTools) in PBS for the quantitative analysis of Tspan4a protein. Equal amounts of protein were separated by 12% SDS–PAGE and the corresponding bands were cut out for in-gel digestion. After digestion, the tryptic peptides and standard peptide (sequence: DLYAQN) were labelled with TMT reagents and mixed together. The mixture was desalted using C18 stage tips.

For the liquid chromatography with tandem mass spectrometry (LC–MS/MS) analysis, the peptides were separated by a C18 column (75 µm inner diameter, 150 mm length, 5 µm, 300 Å) with a Thermo-Dionex Ultimate 3000 HPLC system that was directly connected with a Thermo Scientific Q-Exactive HF-X Hybrid Quadrupole-Orbitrap mass spectrometer. A series of adjusted linear gradients according to the hydrophobicity of the fractions with a flow rate of 400 nl min^{-1} was applied. The mass spectrometer was programmed to acquire in the data-dependent acquisition mode. The survey scan was from m/*z* 300 to 1,800 with a resolution of 60,000 at m/*z* 400. After one microscan, the top 40 most-intense peaks with a charge state of two and above were dissociated by normalized collision energy of 32%. The isolation window was set at a 1-Da width and the dynamic exclusion time was 15 s. The MS/MS spectra were acquired with a resolution of 15,000, AGC target of 1×10^5 and maximum injection time of 50 ms.

The generated MS/MS spectra were searched against the Uniprot zebrafish database using the SEQUEST search engine with Proteome Discoverer 2.2 software. The search criteria were as follows: full tryptic specificity was required, one missed cleavage was allowed, carbamidomethylation on cysteine and TMT sixplex on lysine/peptide N terminals were set as the fixed modifications, oxidation on methionine was set as the variable modification, precursor-ion mass tolerances were set at 20 ppm for all mass spectrometry acquired in an Orbitrap mass analyzer and the fragment-ion-mass tolerance was set to 20 mmu for all MS/MS spectra acquired. Peptide spectral matches were validated using the Percolator provided by Proteome Discoverer software based on the *q* values at a 1% false discovery rate. Proteomic analysis was carried out in biological triplicates.

Antibodies. The anti-Cxcl12a (zebrafish) antibody was generated by Abgent Biotechnology (Suzhou) Co., Ltd. Anti-Integrin β1b (zebrafish) was a gift from J. Xiong. Other antibodies have been specified in the Reporting Summary.

Whole-mount immunofluorescence. For the staining of zebrafish KVs, embryos at the six-somite stage (12 h.p.f.) were first fixed in 4% paraformaldehyde for 2 d at 4 °C. The fixed embryos were then dehydrated using graded methanol and kept in −20 °C methanol overnight. The dehydrated embryos were rehydrated using graded 0.5% PBST (Triton-X 100; Solarbio, 524A0513). The rehydrated embryos were incubated in block solution (1% BSA, 0.3 M glycine and 10% goat serum in 0.5% PBST) for 1 h at room temperature on a slow shaker and then further incubated overnight with primary antibody diluted 1:50 in block solution at 4 °C on a slow shaker. The primary antibody solution was removed and the embryos were washed in 0.5% PBST for at least 3 × 1 h at room temperature on a shaker. Incubation in secondary antibody (diluted 1:200 in block solution) was carried out overnight at 4 °C on a slow shaker. The embryos were washed in 0.5% PBST as before and finally mounted in 1% low-melting-point agarose for imaging. The primary antibodies used were rabbit anti-αPKC (1:50; sc-216, Santa Cruz) and mouse anti-acetylated tubulin (1:50; T6793, Sigma). The secondary antibodies were Alexa Fluor 488-conjugated anti-rabbit IgG (1:200; A11008, Invitrogen) and Alexa Fluor TRITC-conjugated anti-mouse IgG (1:200; 81–6514, Invitrogen).

To stain endogenous Cxcl12a and Integrin β1b in zebrafish whole-mounts, a single blastomere of embryos at the eight-to-sixteen-cell stage was injected with 300 pg *tspan4a–GFP* or *PH–GFP* mRNA. The embryos were fixed at the 75% epiboly stage using methanol at −20 °C after removing the chorion. The fixed embryos were then dehydrated overnight in fresh methanol in a −20 °C freezer. Rehydration and staining were performed using the same protocol as for KV staining. The primary antibodies used were rabbit anti-Cxcl12a antibody (Abgent Biotechnology (Suzhou) Co., Ltd), rabbit anti-Integrin β1b from J. Xiong and chick anti-GFP (Abcam, ab13970). The secondary antibodies were anti-rabbit TRITC/647 and anti-chick 488 (Abcam, ab150169).

Cell immunofluorescence. MGC803 cells (or zebrafish primary cells) were cultured in confocal dishes coated with fibronectin (PHE0023, Life Technologies). The cells were washed with PBS, fixed in methanol (pre-cooled to −20° C) for 15 min, washed three times with PBS, and permeabilized and blocked in blocking buffer (0.1% saponin and 10% fetal bovine serum in PBS) for 30 min. The cells were then stained with primary antibody (1:100; 10 µg ml^{-1}) in blocking buffer for 1 h, washed three times with PBS, stained with secondary antibody in blocking buffer for 1 h and finally washed three more times with PBS.

Transplantation assay. For the DFC transplantations, DFCs from shield-stage *Tg(sox17:GFP)* embryos were transplanted into the DFC region of WT, *MZtspan4a* and *MZtspan7* embryos at the same stage. The acceptor embryos were injected with approximately 300 pg *nls*–mCherry mRNA at the single-cell stage before transplantation to label all blastoderm cells. About 1 h post-transplantation, the acceptor embryos were mounted in 1% low-melting-point agarose and observed for at least 12 h with a light-sheet microscope.

Expression vectors. For mRNA synthesis, the coding sequence of each gene was synthesized (Wuxi Qinglan Biotech Co., Ltd) and inserted into mCherry- or GFP-tagged pXT7. All mRNAs were synthesized using the mMessage mMachine T7/SP6 kit (AM1344, Ambion).

For the cell transfections, TSPAN4–mCherry and PH–mCherry were cloned into the pmCherry-N1 vector.

Cell culture and transfection. MGC803 and L929 cells were cultured in DMEM (Life Technologies) supplemented with 10% fetal bovine serum (5% CO_2). The cells were transfected with 2 μg DNA via Amaxa nucleofection using solution T and program X-001.

Zebrafish primary cells were isolated from gastrulas and cultured in Leibovitz's L-15 medium supplemented with 15% fetal bovine serum, 100 U ml^{-1} penicillin and 10 mg ml^{-1} streptomycin. The cells were cultured in fibronectin-coated dishes for 24 h and prepared for immunofluorescence staining or time-lapse imaging.

Imaging. To acquire two-dimensional images and living two-dimensional images of embryos, mRNA was injected at the desired embryonic stage (or immunofluorescence stained embryo *z*-stack images), the embryos were then embedded in 1% low-melting-point agarose and imaged by Olympus FV1200 confocal microscopy.

To acquire living-embryo *z*-stack images for the statistical analysis of migrasomes (Fig. 2), mRNA was injected at the desired embryonic stage. The embryos were embedded in 1% low-melting-point agarose and *z*-stack imaging was performed (2 μm × 25 slices × 9 views) by spinning disk microscopy (Perkin Elmer).

To acquire time-lapse multiple-view *z*-stack images (4D imaging), embryos were embedded in 1% low-melting-point agarose and imaged by Zeiss light-sheet Z.1 microscopy.

To acquire images of FISH-treated 48 h.p.f. embryos, embryos were embedded in 1% low-melting-point agarose and imaged by Zeiss light-sheet Z.1 microscopy.

To visualize the embryonic shield cavity in shield-stage embryos, fluorescently labelled dextrans (Invitrogen, D22914) were injected at the 50% epiboly stage, *tspan4a–GFP* mRNA was injected at the eight-cell stage and purified migrasomes stained with CM-DiI were injected at the 50% epiboly stage. *Z*-stack imaging of the embryos was performed by Zeiss light-sheet Z.1 microscopy.

Image processing. All of the time-lapse multiple-view *z*-stack embryo images (4D images) were processed using Imaris software 8.1.4 (Bitplane AG).

Images were processed by Image J to quantify the fluorescence intensity, vesicle size and the area covered by the DFCs.

To determine the cell migration direction and the retraction-fibre direction, time-lapse images were acquired by Olympus FV1200 confocal microscopy and analysed using Imaris software 8.1.4.

To determine the migration speed of embryonic cells, embryos were injected with *nls–mCherry* mRNA at the single-cell stage and 4D imaging was performed from the shield stage to the bud stage. The images were analysed using Imaris software 8.1.4.

For the embryos labelled with the six primordial organ markers, images were processed for 3D surface reconstruction with different colours using Imaris software 8.1.4.

Migrasome purification. Migrasome purification was performed by iodixanol-sucrose density gradient centrifugation using an Optiprep kit (LYSISO1, Sigma-Aldrich). Blastoderms of zebrafish embryos (approximately 5,000 embryos for the rescue experiment and 20,000 embryos for quantitative mass spectometry analysis) at the gastrulation stage were collected and resuspended in Ringer's solution (6.786 g l^{-1} NaCl, 0.216 g l^{-1} KCl and 1.19 g l^{-1} HEPES, pH 7.2). The samples were then centrifuged at 1,000*g* for 10 min at 4 °C, followed by 2,000*g* for 10 min at 4 °C to remove the cell body and finally at 20,000*g* for 20 min at 4 °C. The pellet containing the crude migrasome fraction was resuspended and lysed in extraction buffer (Sigma-Aldrich) and then fractionated at 150,000*g* for 4 h at 4 °C in a multi-step Optiprep dilution gradient. The gradient was: 3, 5, 8, 12, 16, 19 (sample), 22.5 and 25%. The respective gradient volumes were: 300, 300, 300, 900, 1,000, 800, 500 and 300 μl. For fractions 3–5, 500 μl was collected and added to 500 μl PBS. Centrifugation was then performed at 20,000*g* for 20 min at 4 °C. The pellet was collected, washed once with PBS and centrifuged at 4 °C, 2,000*g* for 10 min. The supernatant was collected and centrifuged at 4 °C, 20,000*g* for 20 min to obtain migrasomes for TEM observation and injection into embryos.

Preparation of agarose-embedded migrasomes and migrasome injection. For the chemoattractant assays, purified migrasomes (from approximately 5,000 gastrulas) were resuspended in 5 μl PBS and added to 5 μl 2% low-melting-point agarose, which contained fluorescent beads for tracing. This mixture was then injected (approximately 5 nl) into the ventral side of *Tg(sox17:GFP)* embryos at the shield stage.

For the migrasome rescue experiments, purified migrasomes (from approximately 5,000 embryos) were resuspended in 5 μl PBS and injected into mutant embryos (approximately 10 nl) at 30–50% epiboly.

TEM. Shield-stage embryos were fixed with 2.5% glutaraldehyde + 2.0% paraformaldehyde diluted in 0.1 M PB buffer, pH 7.4. The embryos were kept at room temperature for 2 h and then at 4 °C overnight. After three 10 min washes with PB (0.1 M), the embryos were treated with 1.5% $K_3Fe(CN)_6$ + 1% OsO_4 (mixed before use) and kept at 4 °C for 1.5 h. The embryos were washed three times with ddH_2O (10 min each wash), and then treated with 1% uranyl acetate in water and kept at 4 °C overnight. After three 10 min washes in ddH_2O, the samples were dehydrated in ethanol (50, 70, 80, 90, 100, 100 and 100%; 10 min each), treated with 100% ethanol:100% acetone at a 1:1 ratio for 8 min, followed by 100% acetone for 8 min. The embryos were infiltrated with PON 812 resin as follows: 1:1 resin:acetone, 2 h at room temperature; 2:1 resin:acetone, 2 h at room temperature; 3:1 resin:acetone, 2 h at room temperature; resin alone, overnight and resin alone, 2 h. The embryos were then placed in the correct orientation on a 3.5-mm culture dish and a capsule filled with resin was placed over the embryo. The resin was polymerized at 37 °C for 8 h, 45 °C for 24 h and 60 °C for 12 h. Sections (70 nm) were cut with a Leica EM UC7 microtome and then stained with uranyl acetate and lead citrate. Images were obtained with a H-7650B TEM at 80 KV.

Statistics and reproducibility. The statistical analysis in Fig. 4e and Supplementary Table 1 was performed by Excel using a two-tailed, two-sample unequal variance *t*-test. The precise *P* values have been indicated in the legends and Supplementary Table 1. All other statistical analyses were performed using GraphPad Prism5 software. The error bars in Fig. 3c,d,g,h and Supplementary Figs. 4c,d, 5f–i represent the mean ± s.d. All other error bars in the figures represent the mean ± s.e.m. Comparisons were performed by two-tailed, unpaired Student's *t*-tests. $P < 0.05$ was considered statistically significant. A description of each statistical test and the *n* and *P* values are included with each legend or experimental source data (Supplementary Table 3). The number of experimental repeats are specified in the figure legends. The experiments in Figs. 2b, 3a, 6a, Supplementary Figs. 1m,n, 2g–j, 3a–e, 4a,b,e, 5a–c, 7a,b and Supplementary Videos 4,10 were conducted once. The experiments in Figs. 1i,k, 4c,f, 7a–c,h, Supplementary Figs. 1a–g,j–l, 2a,e,f, 5e and Supplementary Videos 2,5,7 were performed twice independently with similar results. The experiments in Figs. 1g, 2g and Supplementary Fig. 2d were pooled from two independent experiments. The experiments in Figs. 1d,h, 2d,f, 4e, 5b,c,e,f,h,i, 6c,d, 7f,g and Supplementary Figs. 1i, 2c, 6b were pooled from three independent experiments. All other experiments were performed three independent times with similar results.

Reporting Summary. Further information on research design is available in the Nature Research Reporting Summary linked to this article.

Data availability

RNA sequencing data that support the findings of this study have been deposited in the National Center for Biotechnology Information Sequence Read Archive under the accession codes SRR9047069 and SAMN11633758.
The mass spectrometry proteomics data have been deposited to the ProteomeXchange Consortium via the PRIDE partner repository with the dataset identifier PXD013835. The statistical source data for Figs. 1–3,5–7 and Supplementary Figs. 1–6 have been provided as Supplementary Table 3. All other data supporting the findings of this study are available from the corresponding author on reasonable request. Further information and requests for resources and reagents should be directed to and will be fulfilled by L. Yu.

References

18. Zhang, J., Jiang, Z., Liu, X. & Meng, A. Eph/ephrin signaling maintains the boundary of dorsal forerunner cell cluster during morphogenesis of the zebrafish embryonic left-right organizer. *Development* **143**, 2603–2615 (2016).
19. Huang, P. et al. Heritable gene targeting in zebrafish using customized TALENs. *Nat. Biotechnol.* **29**, 699–700 (2011).
20. Yan, L. et al. Maternal Huluwa dictates the embryonic body axis through beta-catenin in vertebrates. *Science* **362**, eaat1045 (2018).
21. Thisse, C. & Thisse, B. High-resolution in situ hybridization to whole-mount zebrafish embryos. *Nat. Protoc.* **3**, 59–69 (2008).
22. Brend, T. & Holley, S. A. Zebrafish whole mount high-resolution double fluorescent in situ hybridization. *J. Vis. Exp.* **25**, e1229 (2009).
23. Gong, B. et al. The Sec14-like phosphatidylinositol transfer proteins Sec14l3/SEC14L2 act as GTPase proteins to mediate Wnt/Ca^{2+} signaling. *eLife* **6**, e26362 (2017).

nature research

Corresponding author(s): Li Yu, Anming Meng

Last updated by author(s): 2019-6-6

Reporting Summary

Nature Research wishes to improve the reproducibility of the work that we publish. This form provides structure for consistency and transparency in reporting. For further information on Nature Research policies, see Authors & Referees and the Editorial Policy Checklist.

Statistics

For all statistical analyses, confirm that the following items are present in the figure legend, table legend, main text, or Methods section.

n/a	Confirmed	
☐	☒	The exact sample size (*n*) for each experimental group/condition, given as a discrete number and unit of measurement
☐	☒	A statement on whether measurements were taken from distinct samples or whether the same sample was measured repeatedly
☐	☒	The statistical test(s) used AND whether they are one- or two-sided *Only common tests should be described solely by name; describe more complex techniques in the Methods section.*
☒	☐	A description of all covariates tested
☒	☐	A description of any assumptions or corrections, such as tests of normality and adjustment for multiple comparisons
☐	☒	A full description of the statistical parameters including central tendency (e.g. means) or other basic estimates (e.g. regression coefficient) AND variation (e.g. standard deviation) or associated estimates of uncertainty (e.g. confidence intervals)
☐	☒	For null hypothesis testing, the test statistic (e.g. *F*, *t*, *r*) with confidence intervals, effect sizes, degrees of freedom and *P* value noted *Give P values as exact values whenever suitable.*
☒	☐	For Bayesian analysis, information on the choice of priors and Markov chain Monte Carlo settings
☒	☐	For hierarchical and complex designs, identification of the appropriate level for tests and full reporting of outcomes
☒	☐	Estimates of effect sizes (e.g. Cohen's *d*, Pearson's *r*), indicating how they were calculated

Our web collection on statistics for biologists contains articles on many of the points above.

Software and code

Policy information about availability of computer code

Data collection	Images are acquired by FV10-ASW-4.2 (Olympus), FV31S-SW V2.3.1 (Olympus), ZEN 2014 (Zeiss), Volocity 6.3.1 (PerkinElmer).
Data analysis	Imaris 8.1.4 was used for analysis of cell migrate direction, surface processing of FISH images, DFCs movement and migrasomes chemoattractant movie processing. Image J was used for analysis of vesicles diameter, relative intensity and migrasomes accumulation images. Photoshop cc 2018 was used for supplementary videos processing. Proteome Discoverer 2.2 were used for mass spectrum data analysis. GraphPad Prism 5 was used for statistic analysis.

For manuscripts utilizing custom algorithms or software that are central to the research but not yet described in published literature, software must be made available to editors/reviewers. We strongly encourage code deposition in a community repository (e.g. GitHub). See the Nature Research guidelines for submitting code & software for further information.

Data

Policy information about availability of data

All manuscripts must include a data availability statement. This statement should provide the following information, where applicable:

- Accession codes, unique identifiers, or web links for publicly available datasets
- A list of figures that have associated raw data
- A description of any restrictions on data availability

RNA–seq data that support the findings of this study have been deposited in the National Center for Biotechnology Information (NCBI) Sequence Read Archive (SRA) under accession code SRR9047069 and SAMN11633758.
The mass spectrometry proteomics data have been deposited to the ProteomeXchange Consortium via the PRIDE partner repository with the dataset identifier PXD013835.

Statistical source datas for Fig. 1-3, 5-7 and Supplementary Fig. 1-6 have been provided as Supplementary Table 3.
All other data supporting the findings of this study are available from the corresponding author on reasonable request.

Field-specific reporting

Please select the one below that is the best fit for your research. If you are not sure, read the appropriate sections before making your selection.

☒ Life sciences ☐ Behavioural & social sciences ☐ Ecological, evolutionary & environmental sciences

For a reference copy of the document with all sections, see nature.com/documents/nr-reporting-summary-flat.pdf

Life sciences study design

All studies must disclose on these points even when the disclosure is negative.

Sample size	No statistical methods were used to determine sample size. It has been our routine practice to use a suitable number.
Data exclusions	No data were excluded from the analysis.
Replication	Attempts at replication were successful.
Randomization	Microscopic images were acquired randomized on any given slide.
Blinding	The investigators were not blinded to allocation during experiments and outcome assessment.

Reporting for specific materials, systems and methods

We require information from authors about some types of materials, experimental systems and methods used in many studies. Here, indicate whether each material, system or method listed is relevant to your study. If you are not sure if a list item applies to your research, read the appropriate section before selecting a response.

Materials & experimental systems

n/a	Involved in the study
☐	☒ Antibodies
☐	☒ Eukaryotic cell lines
☒	☐ Palaeontology
☐	☒ Animals and other organisms
☒	☐ Human research participants
☒	☐ Clinical data

Methods

n/a	Involved in the study
☒	☐ ChIP-seq
☒	☐ Flow cytometry
☒	☐ MRI-based neuroimaging

Antibodies

Antibodies used

Anti-Zebrafish Cxcl12a (Abgent Biotechnology) N/A
Anti-Zebrafish Integrin β1b (A gift from Jingwei Xiong Laboratory) N/A
Anti-Human Integrin β1 (R&D systems) Clone# 4B7R, Cat# MAB17783, RRID: AB_2129938
Anti-GFP (Santa Cruz), Cat# Sc-9996, RRID: AB_627695
Anti-GFP (Abcam), Cat#ab13970, RRID: AB_300798
Anti-aPKC (Santa Cruz), Cat# Sc-216, RRID: AB_2300359
Anti-acetylated tubulin (Sigma), Cat# T6793,RRID: AB_477585
Anti-Cxcr4b (GeneTex), Cat# GTX132244-S
Anti-Active Caspase-3 (BD Biosciences), Cat# 559565, RRID:AB_397274
Anti-Actin (Zen Bioscience), Cat# 200068-8F10, RRID: AB_2722710
Anti-GAPDH (Proteintech), Cat# 60004-1-Ig, RRID: AB_2107436
Alexa Fluor 488-conjugated anti-rabbit IgG (Invitrogen), Cat# A11008, RRID: AB_143165
Alexa Fluor TRITC-conjugated anti-mouse IgG (Invitrogen), Cat# 81-6514, RRID: AB_87835
Alexa Fluor 488-conjugated anti-chicken IgY H&L (Abcam), Cat# ab150169, RRID:AB_2636803

Validation

Anti-zebrafish Cxcl12a was validated by morpholinos using western blot and immunofluorescence staining (Supplementary Fig. 5b-c).
Anti-zebrafish Integrin β1b was validated by morpholinos using western blot (Supplementary Fig. 4e).
Anti-Human Integrin β1 by the manufacturer using immunofluorescence staining, and we also checking their localization was consistent with literature reports.
Anti-GFP (Santa Cruz) was validated by the manufacturer using western blot and immunofluorescence staining in COS cells.
Anti-GFP (Abcam) was validated by the manufacturer using ICC-IF, IHC, IHC-P, IHC-WM, and WB.
Anti-aPKC was validated by the manufacturer using WB, IP, IF and ELISA. Species: mouse, rat, human. And this antibody has been

validated by previous study using immunofluorescence staining in zebrafish (Zhang J. et al., Development, 2016).
Anti-acetylated tubulin was validated by the manufacturer. Species reactivity: plant, pig, human, monkey, hamster, invertebrates, chicken, bovine, rat, frog, protista, mouse. Application: dot blot: suitable, electron microscopy: suitable, immunocytochemistry: suitable, indirect ELISA: suitable, radioimmunoassay: suitable. And this antibody has been validated by previous study using immunofluorescence staining in zebrafish (Zhang J. et al., Development, 2016).
Anti-zebrafish Cxcr4b was validated by the manufacturer using western blot, and we validated using morpholino and also checking their localization was consistent with literature reports.
Anti-Actin was validated by the manufacturer using western blot. Species reactivity: Human, Mouse, Monkey, Goat, Rat, Hamster, Saccharomyces cerevisiae, Arabidopsis, Pichia pastoris, Rabbit, Zebrafish, Drosophila, Leaf of Rice, Fruit of Cucumber, Chlamydomonas Reinhardtii, Fish, Pig, Chicken.
Anti-Active Caspase-3 was validated by the manufacturer. Species reactivity: Human (QC Testing) Mouse (Tested in Development). Application: Intracellular staining (flow cytometry), Immunoprecipitation/Western blot (Routinely Tested), ELISA, Bioimaging, Immunohistochemistry-frozen (Tested During Development).
Anti-GAPDH was validated by the manufacturer using western blot. Species reactivity: human, mouse, rat, zebrafish, yeast, plant, beagle, carp, chicken, cow, Cynomorium songaricum Rupr, Cyprinus carpio, deer, dog, Eelworm, H. illucens.
The antibody dilution ratio has been specified in methods.

Eukaryotic cell lines

Policy information about cell lines

Cell line source(s)	Human MGC803 (a gift from Zhijie Chang laboratory, Tsinghua University), RRID: CVCL_5334 Mouse L929 (ATCC), CCL-1, RRID:CVCL_0462 Human BT549 (ATCC), Cat# HTB-122, RRID: CVCL_1092 Rat NRK (ATCC), Cat# CRL-6509, RRID:CVCL_3758
Authentication	The cell lines were not authenticated.
Mycoplasma contamination	The cell line were not tested for mycoplasma contamination.
Commonly misidentified lines (See ICLAC register)	No cell lines used in this study were found in the database of commonly misidentified cell lines that is maintained by ICLAC and NCBI Biosample.

Animals and other organisms

Policy information about studies involving animals; ARRIVE guidelines recommended for reporting animal research

Laboratory animals	Zebrafish strains used in this study are: Tübingen Tg(sox17:GFP)s870, s870Tg, Navis et al., 2013, ZFIN ID: ZDB-FISH-150901-29329 itgb1b mutant (56-bp deletion and 1-bp insertion) Jingwei Xiong Laboratory, Peking University, China tspan4a mutant (2-bp deletion), This paper tspan7 mutant (10-bp insertion), This paper cxcl12a mutant (4-bp deletion), This paper cxcr4b mutant (4-bp deletion), Feng Liu Laboratory, Institute of Zoology (IOZ), Chinese Academy of Sciences (CAS) Both males and females between 3-12 month were used to produce embryos.
Wild animals	None of the wild animals used
Field-collected samples	This study did not involve samples collected from field
Ethics oversight	Use of all zebrafish adults and embryos was according to the guidelines from the Animal Care and Use Committee of Tsinghua University.

Note that full information on the approval of the study protocol must also be provided in the manuscript.